Bull Math Biol (2017) 79:389–429
DOI 10.1007/s11538-016-0237-2

Society for Mathematical Biology

ORIGINAL ARTICLE

A Multiscale Mathematical Model of Tumour Invasive Growth

Lu Peng[1,2] · Dumitru Trucu[1] · Ping Lin[1] · Alastair Thompson[3] · Mark A. J. Chaplain[4]

Received: 27 June 2015 / Accepted: 2 December 2016 / Published online: 16 February 2017

Abstract Known as one of the hallmarks of cancer (Hanahan and Weinberg in Cell 100:57–70, 2000) cancer cell invasion of human body tissue is a complicated spatio-temporal multiscale process which enables a localised solid tumour to transform into a systemic, metastatic and fatal disease. This process explores and takes advantage of the reciprocal relation that solid tumours establish with the extracellular matrix (ECM) components and other multiple distinct cell types from the surrounding microenvironment. Through the secretion of various proteolytic enzymes such as matrix metalloproteinases or the urokinase plasminogen activator (uPA), the cancer cell population alters the configuration of the surrounding ECM composition and overcomes

✉ Dumitru Trucu
trucu@maths.dundee.ac.uk

Lu Peng
penglu@csrc.ac.cn

Ping Lin
plin@maths.dundee.ac.uk

Alastair Thompson
AThompson1@mdanderson.org

Mark A. J. Chaplain
majc@st-andrews.ac.uk

1 Division of Mathematics, University of Dundee, Dundee DD1 4HN, UK

2 Present Address: Division of Applied and Computational Mathematics, Beijing Computational Science Research Centre, 10 Dongbeiwang West Road, Haidian District, Beijing 100193, China

3 MD Anderson Cancer Center, The University of Texas, 1515 Holcombe Blvd, Houston, TX 77030, USA

4 School of Mathematics and Statistics, Mathematical Institute, University of St Andrews, St Andrews KY16 9SS, UK

the physical barriers to ultimately achieve local cancer spread into the surrounding tissue. The active interplay between the tissue-scale tumour dynamics and the molecular mechanics of the involved proteolytic enzymes at the cell scale underlines the biologically multiscale character of invasion and raises the challenge of modelling this process with an appropriate multiscale approach. In this paper, we present a new two-scale moving boundary model of cancer invasion that explores the tissue-scale tumour dynamics in conjunction with the molecular dynamics of the urokinase plasminogen activation system. Building on the multiscale moving boundary method proposed in Trucu et al. (Multiscale Model Simul 11(1):309–335, 2013), the modelling that we propose here allows us to study the changes in tissue-scale tumour morphology caused by the cell-scale uPA microdynamics occurring along the invasive edge of the tumour. Our computational simulation results demonstrate a range of heterogeneous dynamics which are qualitatively similar to the invasive growth patterns observed in a number of different types of cancer, such as the tumour infiltrative growth patterns discussed in Ito et al. (J Gastroenterol 47:1279–1289, 2012).

Keywords Cancer invasion · Multiscale modelling · uPA system

1 Introduction

Cancer is a complicated disease that involves many cross-related processes occurring over several spatial scales, ranging from genes to cells to tissues. The abilities of cancer cells to activate invasion and metastasis, to sustain proliferative signalling, to evade growth suppressors, to enable replicative immortality, to induce angiogenesis and to resist cell death have been initially identified as the six main hallmarks of cancer (Hanahan and Weinberg 2000). A growing knowledge about cancer over the last decade has shed more light on the whole picture of the disease, and another four hallmarks were added, namely the ability of cancer to avoid immune destruction, to deregulate cellular energetics, to develop tumour-promoting inflammations, alongside genome instability and mutations (Hanahan and Weinberg 2011).

Highlighted as one of the hallmarks of cancer, cancer cell invasion is a landmark event that transforms a locally growing tumour into a systemic, metastatic and fatal disease. The past four decades have witnessed great scientific efforts focussed on gaining a better understanding of the processes involved during cancer invasion, which is of highly importance in designing early detection strategies and attempting effective therapies.

A malignant tumour includes a complex heterotypic community of cells (such as cancer cells, immuno-inflammatory cells, stromal cell, fibroblasts, endothelial cells and macrophages) that are mixed with ECM. This community is enhanced by vastly complex signalling pathways underpinning intense molecular processes that mediates the crosstalk between the various cell populations composing the tumours, such as the interaction between the cancer cells and the peritumoural stroma cells occurring during cancer invasion (Hanahan and Weinberg 2011; E and Engquist 2003; Qian and Pollard 2010; Joyce and Pollard 2009; Kalluri and Zeisberg 2006). As one of the main factors that affect the way the cancer cell migrate and invade, the peritumoural ECM not only

plays the role of a scaffold for the tissues and physical barriers during cell migration but also conveys the signalling pathway processes, enabling the cells to communicate. These give rise to specific conditions within the tumour microenvironment that locally regulate cell migration, proliferation and differentiation. Specifically, the secretion of proteolytic enzymes such as urokinase plasminogen activator (uPA) and matrix metalloproteinases (MMPs) by the tumour cells and interactions of these enzymes with the ECM components lead to proteolytic degradation and remodelling of the ECM and represent a key step in the cancer invasion process.

In order to decipher the mechanisms behind the complicated processes involved in cancer invasion, clinical investigations and experimental observations carried out over the past few decades have started being increasingly accompanied by mathematical modelling (Adam 1986; Anderson et al. 2000; Byrne and Chaplain 1996; Chaplain et al. 2006; Gatenby and Gawlinski 1996; Greenspan 1976; Perumpanani et al. 1996, 1998; Webb et al. 1999). These initial modelling attempts used reaction-diffusion systems to describe the interaction between malignant and normal cells and focused on several important invasion aspects, leading to the first qualitative mathematical modelling approaches and paving the way towards a better understanding of the contribution of proteolytic enzymes in cancer invasion. This was further explored with modelling focused the role of proteolytic activities of some specific hydrolytic enzymes such as urokinase plasminogen activator (uPA) and matrix metalloproteinases (MMPs) in tumour invasive behaviour (Andasari et al. 2011; Anderson 2005; Byrne et al. 2001; Chaplain and Lolas 2005; Deakin and Chaplain 2013; Perumpanani et al. 1996, 1998). For instance, while Chaplain and Lolas (2005) proposed a system of reaction–diffusion–taxis partial differential equations to explore the role of the uPA system (including uPA, uPA-inhibitors, plasmin and host tissue) in cancer invasion, the model introduced in Deakin and Chaplain (2013) evaluates the role of two types of simultaneously expressed MMPs on cancer growth and spread, i.e. membrane-bound matrix MT1-MMP and soluble MMP-2.

Alongside the chemotactic and haptotactic movement assumed in all the models mentioned above, cell–cell and cell-matrix adhesion were also recognised as playing a crucial role in the growth and development of carcinomas (Byrne and Chaplain 1996). Advances in addressing the importance of cell adhesion in the cancer invasion process were obtained via several models based on systems of non-local integro-differential equations (Armstrong et al. 2006; Chaplain et al. 2011; Domschke et al. 2014; Gerisch and Chaplain 2008) that account for dynamic interactions within an appropriately small sensing radius R between potentially mutating cancer cell populations, ECM, and the involved matrix degradation enzymes.

Since the local tissue invasion of a malignant tumour could be regarded also as a free moving boundary problem, several appropriate numerical techniques were considered in the computational modelling of cancer invasion. Particularly, the level-set method was intensely used to study solid tumour growth in homogeneous microenvironments (Frieboes et al. 2006; Macklin and Lowengrub 2005, 2006, 2007; Zheng et al. 2005). A new ghost cell/level- set method (based on a nonlinear nutrient equation coupled with a pressure equation with geometry-dependent jump boundary conditions) was developed in Macklin and Lowengrub (2008) and applied to models of tumour invasive growth in complex, heterogeneous tissues. This model was later extended into an

improved model of tumour invasion including the process of tumour-induced angiogenesis (Macklin et al. 2009). Finally, alongside the level-set method, multiphase models based on the theory of mixtures were also developed and used to investigate tumour growth and spread (Byrne and Preziosi 2003; Chaplain et al. 2006; Frieboes et al. 2010; Preziosi and Tosin 2009; Wise et al. 2008, 2011). In these approaches, the tumour was regarded as a system consisting of different phases (e.g. cellular phase, liquid phase) and the development of a solid tumour was modelled by exploring the mass and momentum balances alongside the constitutive laws that distinguish the phases in the system.

However, while recognising the multiscale nature of cancer growth and spread, over the past two decades or so most computational and mathematical modelling has focused mainly on one scale, either at the tissue, cell or molecular scale, with the first attempts towards linking these scales being revised in Deisboeck et al. (2011). Recently, following a series of important developments within the general multiscale framework, and based on strong insights from atomistic-to-continuum methods (Lin 2007), homogenisation techniques (Allaire 1992; Trucu et al. 2012), and heterogeneous multiscale finite element methodology (Abdulle and Schwab 2005; E and Engquist 2003; Ren and E 2005), a genuinely new multiscale moving boundary model for cancer invasion that links the tissue, cellular and subcellular scales was proposed in Trucu et al. (2013). In this new framework, PDE modelling at the tissue scale for the cell population dynamics and PDE modelling at the cell scale for the molecular mechanics of the proteolytic enzymes population are linked together in a two-scale model through top-down and bottom-up permanent links. The top-down link provides the source for the microscale dynamics, which is induced in a non-local manner by the macrodynamics. On the other hand, the bottom-up link enables the microdynamics to provide the macrodynamics with a law for the macroscale boundary movement, whose direction and displacement magnitude is determined at microscale. This is fundamentally different from previous modelling perspectives such as the one-scale modelling presented in Anderson et al. (2000), or the one proposed in Ramis-Conde et al. (2008) where the authors considered continuous modelling at the microscale but an individual-based model at the macroscale and where no top-down links were assumed.

In this paper, we propose a novel multiscale mathematical model of cancer invasion that explores the tissue-scale cancer progression in conjunction with the cell-scale dynamics of the urokinase plasminogen activation system. Building on the multiscale moving boundary method proposed in Trucu et al. (2013), the new modelling that we propose here allows us to study the changes in tissue-scale (macro) tumour morphology caused by the cell-scale uPA microdynamics occurring in a cell-scale (micro) neighbourhood of the invasive edge of the tumour. Assuming the uPA model developed in Andasari et al. (2011) and Chaplain and Lolas (2005) for the tissue-scale dynamics, we derive governing laws for the degrading enzymes cell-scale dynamics arising in the close proximity of the tumour interface. While this results in prescribing an appropriate form for the top-down link between the macro and microdynamics, by exploring the spatial interaction between the uPA microdynamics and the surrounding ECM from the peritumoural region we obtain a bottom-up link between the micro- and macrodynamics. This allows us to describe the evolution of tumour invasive edge

morphology and enables computational predictions for the changes occurring in the macroscopic pattern of cancer during the local invasion process.

2 Biological Background: Components of the uPA System and Their Functions

Proteolytic degradation and remodelling of the extracellular matrix are essential for cancer cell invasion. It enables cancer cells to proliferate and migrate through surrounding tissue. In this context, one of the first steps of invasion is the production and secretion of proteolytic enzymes, i.e. urokinase plasminogen activator (uPA) and matrix metalloproteinases (MMPs) by cancer cells. These enzymes interact with the dynamics of the ECM macromolecules and pave the way for cancer invasion. Specifically, the uPA enzymatic system mainly consists of the urokinase receptor (uPAR), urokinase plasminogen activator (uPA), the matrix-like protein vitronectin (VN), plasminogen activator inhibitor type-1 (PAI-1) and the degrading enzyme plasmin. Here we list the key activities of the main components of the uPA system and the role each plays in cancer invasion (Andreasen et al. 2000, 1997; Dass et al. 2008; Tang and Han 2013).

2.1 Urokinase Plasminogen Activator (uPA)

uPA is an extracellular serine protease produced by cells. Two major functional domains of the uPA molecule are the protease domain and the growth factor domain. The protease part activates plasminogen and turns it into plasmin, which is able to digest basement membrane and extracellular matrix proteins. The growth factor domain has no protease activity but can bind a specific high-affinity cell-surface receptor, uPAR. Finally, uPA has a zymogen form, pro-uPA, which can be activated by plasmin and binds to uPAR.

2.2 Urokinase Plasminogen Activator Receptor (uPAR)

uPAR is a high-affinity cell-surface receptor of uPA (and of its zymogen form pro-uPA), which via the binding process localises the uPA and pro-uPA to the cell surface. Importantly, uPAR contains another binding site for the ECM component called vitronectin (VN), and since VN and uPA binding sites are distinct, uPAR can simultaneously bind both ligands, allowing coordinated regulation of proteolysis, cell adhesion and signalling.

uPAR expression during ECM remodelling is well controlled under normal conditions, for example, in gestational tissues during embryo implantation and placental development and in keratinocytes during epidermal would healing. uPAR is also expressed in many human cancers. It indicates poor prognosis and in some cases is predictive of invasion and metastasis. Importantly, uPAR expression in tumours can occur in tumour cells and/or tumour-associated stromal cells, such as fibroblasts and macrophages. Moreover, there is a certain crosstalk between these two binding

processes, as the ligand binding of uPA to uPAR enhances the VN binding by uPAR (Smith and Marshall 2010).

2.3 Vitronectin (VN)

VN is an abundant versatile glycoprotein found in serum and the ECM and promotes cell adhesion and spreading. Vitronectin binds strongly to glass surfaces, as the name indicates (vitro = glass), and it has binding sites for several ligands, including heparin, urokinase plasminogen activator receptor (uPAR), plasminogen activator inhibitor type-1(PAI-1) and integrins, such as $\alpha_v\beta_3$. When vitronectin binds to uPAR, it is thought to bring PAI-1 closer to uPA, thereby promoting inhibition and clearance of uPA from the receptor.

2.4 Urokinase Plasminogen Activator Inhibitor-1(PAI-1)

One of the inhibitors of urokinase plasminogen activator, PAI-1, belongs to the serpin (serine protein inhibitors) family, and it is believed to be the most abundant, fast-acting inhibitor of uPA in vivo. It can specifically bind to soluble and membrane-bound uPA to inhibit plasminogen activation. When PAI-1 binds to the uPA/uPAR complex, it triggers the internalisation of the uPA/uPAR/PAI-1 complex by receptor-mediated endocytosis, meaning that the complex will be dissociated and PAI-1 and uPA will be digested, but the receptor will be recycled to the cell surface. This process helps with the clearance of PAI-1 from the vicinity of the cell surface. Additionally, as a major binding protein of VN, PAI-1 competes with uPAR for binding to VN.

2.5 Plasmin

Plasmin is a widespread enzyme that cleaves many extracellular matrix proteins, such as fibronectin, laminin, vitronectin and thrombospondin. In addition, plasmin can also activate many matrix metalloproteinases (MMPs), enhancing even more the degradation of extracellular matrix. It can also influence the composition of the extracellular environment by affecting the activity of cytokines and growth factors, for example, decreasing the activation of TGF-β1 (Venkatraman et al. 2012).

3 Mathematical Modelling

In this section, we will detail the three main components of the uPA multiscale model that we propose for cancer invasion, namely the macroscopic dynamics, the microscopic dynamics and regulation of the tumour boundary relocation. Thus, the description will cover the model at both the macrolevel (tissue scale) and the microlevel (cell scale) and will explore the link between these two biological scales.

3.1 The Macroscopic Dynamics

For the tumour macroscopic dynamics, we adopt here the modelling hypotheses formulated in Andasari et al. (2011) and Chaplain and Lolas (2005) which are based on the activities of the key molecules of the uPA system and their invasive roles (Andreasen et al. 2000, 1997; Dass et al. 2008; Tang and Han 2013).

We denote the cancer cell density by c, the extracellular matrix density by v (without making the distinction between ECM and its component VN), the urokinase plasminogen activator (uPA) concentration by u, the plasminogen activator inhibitor (PAI-1) concentration by p and the plasmin concentration by m. Further, since we assume a fixed average number of receptors uPAR located on each cancer cell surface, there is no explicit modelling of uPAR. Therefore, the concentration of uPAR is considered to be proportional to the cancer cell density. Another important assumption is that the supply of plasminogen is unlimited in this model. Finally, the macroscopic model is obtained by accounting for the biological considerations described in previous section in conjunction with the following presumptions:

3.1.1 The Cancer Cell Dynamics

It is assumed that cancer cell migration is mainly governed by diffusion, chemotaxis due to uPA, and PAI-1 (Degryse et al. 2001; Resnati et al. 2002; Roussos et al. 2011) and haptotaxis due to VN and other ECM components. Additionally, a logistic growth law is used to model cancer cell proliferation. Thus, the mathematical equation for cancer cell density that is considered here is as follows:

$$\frac{\partial c}{\partial t} = \underbrace{D_c \Delta c}_{\text{diffusion}} - \nabla \cdot [\underbrace{\chi_u c \nabla u}_{\text{uPA-chemo}} + \underbrace{\chi_p c \nabla p}_{\text{PAI-1-chemo}} + \underbrace{\chi_v c \nabla v}_{\text{VN-hapo}}] + \underbrace{\mu_1 c(1 - \frac{c}{c_0})}_{\text{profieration}}, \qquad (1)$$

where D_c is the diffusion coefficient of cancer cells, χ_u and χ_p are the chemotaxis coefficients relevant to uPA and PAI-1, respectively, χ_v is the VN-mediated haptotaxis rate, μ_1 is the cancer cell proliferation rate and c_0 is the maximum carrying capacity for cancer cells.

3.1.2 The ECM/VN Dynamics

As ECM is not assumed to move, we rule out any migration terms in the governing law. While VN (which is an important ECM component) is degraded in contact with enzymes m, the binding of PAI-1 to uPA inhibits the activation of plasminogen, leading to the protection of VN and other ECM molecular constituents and indirectly contributing to their production. Simultaneously, the binding of PAI-1 to VN results in less binding to cell-surface receptors such as uPAR, and so, through the regulation of cell-matrix-associated signal transduction pathways, this inhibits the production of VN. Therefore, assuming a logistic ECM remodelling, the governing equation for ECM is given by

$$\frac{\partial v}{\partial t} = -\underbrace{\delta v m}_{\text{degradation}} + \underbrace{\phi_{21} u p}_{\text{uPA/PAI-1}} - \underbrace{\phi_{22} v p}_{\text{PAI-1/VN}} + \underbrace{\mu_2 v (1 - \frac{v}{v_0})}_{\text{remodelling}}. \tag{2}$$

where δ is the rate of ECM degradation by plasmin, ϕ_{21} is the binding rate of PAI-1 to uPA, ϕ_{22} is the binding rate of PAI-1 to VN and μ_2 is the matrix remodelling rate.

3.1.3 The uPA Dynamics

The mathematical modelling of the uPA concentration dynamics accounts for the following aspects. While being produced by the cancer cells and removed from the system due to its binding with PAI-1 and uPAR, per unit time the uPA exercises a local diffusion. Therefore, this can be formalised mathematically as follows:

$$\frac{\partial u}{\partial t} = \underbrace{D_u \Delta u}_{\text{diffusion}} - \underbrace{\phi_{31} p u}_{\text{uPA/PAI-1}} - \underbrace{\phi_{33} c u}_{\text{uPA/uPAR}} + \underbrace{\alpha_{31} c}_{\text{production}}, \tag{3}$$

where D_u is the diffusion coefficient, ϕ_{31} and ϕ_{33} are binding rates of uPA/PAI-1 and uPA/uPAR accordingly, and α_{31} is the production rate of uPA by the cancer cells.

3.1.4 The PAI-1 Dynamics

Similarly, the equation for PAI-1 simply includes a diffusion term with coefficient D_p, removal caused by binding to uPA and VN with binding rates ϕ_{41} and ϕ_{42}, respectively, and production as a result of plasmin formation at a rate α_{41}. Thus, these considerations lead us to the following governing equation:

$$\frac{\partial p}{\partial t} = \underbrace{D_p \Delta p}_{\text{diffusion}} - \underbrace{\phi_{41} p u}_{\text{uPA/PAI-1}} - \underbrace{\phi_{42} p v}_{\text{PAI-1/VN}} + \underbrace{\alpha_{41} m}_{\text{production}}. \tag{4}$$

3.1.5 The Plasmin Dynamics

The evolution of plasmin concentration is modelled as follows. While assuming that per unit time this exercises a local diffusion, we consider that the binding of uPA to uPAR provides an opportunity for pericellular proteolytic activity through plasminogen activation leading to plasmin formation. Moreover, the binding of PAI-1 to VN indirectly enhances the binding of uPA to uPAR, therefore bringing additional contribution to plasmin formation. Thus, these assumptions give us the following evolution law:

$$\frac{\partial m}{\partial t} = \underbrace{D_m \Delta m}_{\text{diffusion}} + \underbrace{\phi_{52} p v}_{\text{PAI-1/VN}} + \underbrace{\phi_{53} c u}_{\text{uPA/uPAR}} - \underbrace{\phi_{54} m}_{\text{degradation}}, \tag{5}$$

where D_m is the diffusion coefficient, ϕ_{52} and ϕ_{53} are the binding rates of PAI-1/VN and uPAR/uPA accordingly and ϕ_{54} is the rate of decay of plasmin.

To summarise the macrodynamics, the dimensionless mathematical model of the uPA system adopted here is the one that was initially proposed in Chaplain and Lolas (2005), namely,

$$\frac{\partial c}{\partial t} = \underbrace{D_c \Delta c}_{\text{diffusion}} - \nabla \cdot [\underbrace{\chi_u c \nabla u}_{\text{uPA-chemo}} + \underbrace{\chi_p c \nabla p}_{\text{PAI-1-chemo}} + \underbrace{\chi_v c \nabla v}_{\text{VN-hapo}}] + \underbrace{\mu_1 c(1-c)}_{\text{profieration}}, \tag{6}$$

$$\frac{\partial v}{\partial t} = - \underbrace{\delta v m}_{\text{degradation}} + \underbrace{\phi_{21} u p}_{\text{uPA/PAI-1}} - \underbrace{\phi_{22} v p}_{\text{PAI-1/VN}} + \underbrace{\mu_2 v(1-v)}_{\text{remodelling}}, \tag{7}$$

$$\frac{\partial u}{\partial t} = \underbrace{D_u \Delta u}_{\text{diffusion}} - \underbrace{\phi_{31} p u}_{\text{uPA/PAI-1}} - \underbrace{\phi_{33} c u}_{\text{uPA/uPAR}} + \underbrace{\alpha_{31} c}_{\text{production}}, \tag{8}$$

$$\frac{\partial p}{\partial t} = \underbrace{D_p \Delta p}_{\text{diffusion}} - \underbrace{\phi_{41} p u}_{\text{uPA/PAI-1}} - \underbrace{\phi_{42} p v}_{\text{PAI-1/VN}} + \underbrace{\alpha_{41} m}_{\text{production}}, \tag{9}$$

$$\frac{\partial m}{\partial t} = \underbrace{D_m \Delta m}_{\text{diffusion}} + \underbrace{\phi_{52} p v}_{\text{PAI-1/VN}} + \underbrace{\phi_{53} c u}_{\text{uPA/uPAR}} - \underbrace{\phi_{54} m}_{\text{degradation}}. \tag{10}$$

We note that the above model was investigated numerically in some depth in Chaplain and Lolas (2005), where wide-ranging computational simulations revealed rich spatio-temporal dynamics. Further numerical investigations on variations of the original model (including a reduced model involving only the three variables c, v, u) were undertaken in Chaplain and Lolas (2006) where once again solutions displaying a persistent "dynamic heterogeneity" were observed. An analysis (linear stability) of the model was later carried out by Andasari et al. (2011) who demonstrated that the dynamic heterogeneous spatio-temporal solutions were caused by a taxis-driven instability of an underlying spatially homogeneous steady state. In particular, three key parameters controlling the bifurcations were noted to be D_c (the cancer cell diffusion coefficient), μ_1 (the cancer cell proliferation rate) and ϕ_{53} (the rate of plasmin production due to uPA/uPAR binding). We also note that a rigorous mathematical analysis of the simplified three-variable system involving only cancer cells, ECM and uPA (i.e. no PAI-1 and no plasmin), was carried out in Hillen et al. (2013) [following a preliminary numerical study in Painter and Hillen (2011)]. This rigorous analysis has shown that the complex dynamics of the model are driven largely by cancer cell proliferation and cancer cell chemotaxis. Finally, we note that a study from a numerical analysis point of view concerning mesh adaptivity has been undertaken in Kolbe et al. (2014).

3.2 The Microscopic Dynamics

Turning now our attention to the microscale setting, in the following we will derive and propose a system of three coupled PDEs to describe the microdynamics of the plasminogen activation system taking place within a cell-scale ϵ-neighbourhood $\mathcal{P}_\epsilon$ of the tumour invasive edge $\partial\Omega(t_0)$ (which is introduced in "Appendix 1").

Assuming that PAI-1 and uPAR are uniformly expressed on the cell surface of various cell types in the tumour, this system will capture the leading edge microdynamics of the uPA, PAI-1 and plasmin by accounting for the following biological considerations. On one hand, the urokinase plasminogen activator (uPA) is assumed to bind to the cancer surface receptor uPAR to activate plasminogen, leading to degradation of pericellular ECM through a series of proteolytic activities. On the other hand, the membrane-bound MMPs (such as MT1-MMP) are secreted from within the tumour cell population distributed on the outer proliferating rim along the entire tumour periphery. Their region of proteolytic activities is therefore restricted around the tumour interface (Deakin and Chaplain 2013; Sabeh et al. 2009). Thus, based on these considerations, we propose a coupled governing law for the leading edge microdynamics, which is detailed as follows:

3.2.1 The uPA Microdynamics

In each microregion ϵY, the dynamics of the uPA molecular population is governed by a diffusion process whose source is induced from the tumour cell macrodynamics. At each point $y \in \epsilon Y$, a source of uPA arises as a collective contribution of the tumour cells distributed within a certain neighbouring area within the tumour's outer proliferating rim. Therefore, this source is denoted by $f_{\epsilon Y}(\cdot,\cdot) \times [0, \Delta t] : \epsilon Y \to \mathbb{R}_+$ and is defined by:

$$f_1^{\epsilon Y}(y,\tau) = \begin{cases} \frac{1}{\lambda(B(y,\gamma)\cap\Omega(t_0))} \int\limits_{B(y,\gamma)\cap\Omega(t_0)} c\ (x, t_0+\tau)\ \mathrm{d}x, & y \in \epsilon Y \cap \Omega(t_0), \\ 0, & \text{outside cancer,} \end{cases} \tag{11}$$

where $\lambda(\cdot)$ is the standard Lebesgue measure and γ represents the maximal thickness of the outer proliferating rim. Thus, per unit time, under the presence of source (11) the uPA is locally diffusing and is binding to both PAI-1 and uPAR, and so its microdynamics can be formally written as:

$$\frac{\partial u}{\partial \tau} = \underbrace{D_u \Delta u}_{\text{diffusion}} - \underbrace{\phi_{31} p u}_{\text{uPA/PAI-1}} + (\underbrace{\alpha_{31}}_{\text{production}} - \underbrace{\phi_{33} u}_{\text{uPA/uPAR}}) f_1^{\epsilon Y}(y,\tau) \tag{12}$$

3.2.2 The PAI-1 Microdynamics

The equation for PAI-1 accounts for diffusive motion, production due to plasmin activation, and loss due to binding with uPA and VN. Specifically, the binding between PAI-1 and VN is as a collective effect of the ECM distribution within ϵY. Therefore, proceeding similarly to the case of the source term in (11), we define

$$f_2^{\epsilon Y}(y,\tau) = \frac{1}{\lambda(B(y,2\epsilon))} \int_{B(y,2\epsilon)} v\ (x, t_0+\tau)\ \mathrm{d}x, \quad y \in \epsilon Y, \tag{13}$$

which finally enable us to write the following governing law for the PAI-1 microdynamics, namely,

$$\frac{\partial p}{\partial \tau} = \underbrace{D_p \Delta p}_{\text{diffusion}} - \underbrace{\phi_{41} p u}_{\text{uPA/PAI-1}} - \underbrace{\phi_{42} p \ f_2^{\epsilon Y}(y,\tau)}_{\text{PAI-1/VN}} + \underbrace{\alpha_{41} m}_{\text{production}} . \tag{14}$$

3.2.3 The Plasmin Microdynamics

For the spatio-temporal evolution of plasmin, it is assumed that, per unit time, this exercises a local diffusion in the presence of the following source and decay circumstances. Considering that the binding of uPA to uPAR is required to provide the cell surface with a potential proteolytic activity, the plasmin source accounts on one hand on the contribution of the binding uPA/uPAR. On the other hand, as PAI-1 collectively competes with uPAR for binding to VN, the binding of PAI-1 to VN gives more opportunities to uPAR to bind with uPA and indirectly results in more plasmin formation. Finally, plasmin can be deactivated either by degradation or by the action of the plasmin inhibitor α_2-antiplasmin. Thus, the equation that we obtain to describe these biological interactions is:

$$\frac{\partial m}{\partial \tau} = \underbrace{D_m \Delta m}_{\text{diffusion}} + \underbrace{\phi_{52} p \ f_2^{\epsilon Y}(y,\tau)}_{\text{PAI-1/VN}} + \underbrace{\phi_{53} u \ f_1^{\epsilon Y}(y,\tau)}_{\text{uPA/uPAR}} - \underbrace{\phi_{53} m}_{\text{degradation}} \tag{15}$$

In summary, the leading edge microdynamics are therefore given by the following system:

$$\frac{\partial u}{\partial \tau} = \underbrace{D_u \Delta u}_{\text{diffusion}} - \underbrace{\phi_{31} p u}_{\text{uPA/PAI-1}} + (\underbrace{\alpha_{31}}_{\text{production}} - \underbrace{\phi_{33} u}_{\text{uPA/uPAR}}) f_1^{\epsilon Y}(y,\tau), \tag{16}$$

$$\frac{\partial p}{\partial \tau} = \underbrace{D_p \Delta p}_{\text{diffusion}} - \underbrace{\phi_{41} p u}_{\text{uPA/PAI-1}} - \underbrace{\phi_{42} p \ f_2^{\epsilon Y}(y,\tau)}_{\text{PAI-1/VN}} + \underbrace{\alpha_{41} m}_{\text{production}}, \tag{17}$$

$$\frac{\partial m}{\partial \tau} = \underbrace{D_m \Delta m}_{\text{diffusion}} + \underbrace{\phi_{52} p \ f_2^{\epsilon Y}(y,\tau)}_{\text{PAI-1/VN}} + \underbrace{\phi_{53} u \ f_1^{\epsilon Y}(y,\tau)}_{\text{uPA/uPAR}} - \underbrace{\phi_{54} m}_{\text{degradation}}. \tag{18}$$

3.3 The Macroscopic Tumour Boundary Relocation Induced by the Leading Edge Microdynamics

Following the multiscale approach described in "Appendix 1", the set of points $\{x^*_{\epsilon Y}\}$ on the boundary of tumour at the current time moves towards a set of new spatial positions $\{\widetilde{x^*_{\epsilon Y}}\}$ to form the new boundary at the next multiscale stage, provided that the local transitional probability q^* is in agreement with the circumstances in the surrounding peritumoural microenvironment. When the invading strength is above a tissue threshold, the point $x^*_{\epsilon Y}$ will relocate to a new position $\widetilde{x^*_{\epsilon Y}}$ following a direction and displacement magnitude that represents the choreographic movement of all the points from the part of the invasive edge captured by the microdomain ϵY.

As described in "The multiscale moving boundary approach for the proposed cancer invasion model" section of "Appendix 1", on any microdomain ϵY, provided that a sufficient amount of plasmin has been produced across the invading edge, it is the pattern of the front of the advancing spatial distribution of plasmin that characterises ECM degradation. Therefore, the movement direction and displacement magnitude of the part of the invading edge of the tumour caputred by the current microdomain ϵY will be determined by the spatial distribution pattern of the advancing front of plasmin $m(\cdot, \tau_f)$ in the peritumoural region. As detailed in "The multiscale moving boundary approach for the proposed cancer invasion model" section of "Appendix 1", these movement characteristics are obtained by accounting the contribution of all peaks (baricentred at the spatial points y_l) at the front of advancing plasmin that are above the mean value of the entire mass of plasmin produced on $\epsilon Y \backslash \Omega(t_0)$ and are located at the furthest away Euclidean distance from $\{x^*_{\epsilon Y}\}$. Thus, under these conditions, the moving direction $\eta_{\epsilon Y}$ and displacement magnitude $\xi_{\epsilon Y}$ derived in "The multiscale moving boundary approach for the proposed cancer invasion model" section of "Appendix 1" in (35)–(36) have the following expressions:

$$\eta_{\epsilon Y} = x^*_{\epsilon Y} + \nu \sum_{l \in \mathcal{I}_\delta} \left(\int_{\mathcal{D}_l} m(y, \tau_f) \mathrm{d}y \right) (y_l - x^*_{\epsilon Y}), \nu \in [0, \infty),$$

$$\xi_{\epsilon Y} := \sum_{l \in \mathcal{I}_\delta} \frac{\int_{\mathcal{D}_l} m(y, \tau_f) \mathrm{d}y}{\sum_{l \in \mathcal{I}_\delta} \int_{\mathcal{D}_l} m(y, \tau_f) \mathrm{d}y} \left| \overrightarrow{x^*_{\epsilon Y} y_l} \right|.$$

Finally, the transitional probability q^* defined in (37) is a quantification of the amount of plasmin in $\epsilon Y \backslash \Omega(t_0)$ relative to the total amount of plasmin concentration in ϵY and characterises the invading strength. Therefore, the point $x^*_{\epsilon Y}$ will exercise the movement into the new spatial position $\widetilde{x^*_{\epsilon Y}}$ if and only if $q(x^*_{\epsilon Y}) := q^*(\epsilon Y)$ exceeds a certain tissue local threshold $\omega(\beta, \epsilon Y) \in (0, 1)$ associated with the microdomain ϵY under a given state of favourable conditions β.

4 Multiscale Computational Simulation Results

The multiscale model of cancer invasion that we proposed here was numerically solved in a rectangular region $Y := [0, 4 \times [0, 4]$. For all our simulations, we discretise the entire cube Y uniformly, using the spatial mesh size: $\Delta x = \Delta y = \frac{\epsilon}{2} = 0.03125$. In this context, the initial conditions for the macrodynamics are specified as follows. The cancer cell population on the initially considered tumour region $\Omega(0) := \mathbf{B}((2, 2), 0.5)$ is assumed to be given by a translated Gaussian centred at $(2, 2)$ and mollified to 0 after a radius of 0.5, namely,

$$c(x, 0) = \frac{\left(\exp\left(- \frac{||x-(2,2)||_2^2}{\sqrt{\Delta x \Delta y}} \right) - \exp(-28.125) \right) \left(\chi_{\mathbf{B}((2,2),0.5-\gamma)} * \psi_\gamma \right)}{2}, \quad x \in Y, \tag{19}$$

where ψ_γ is the mollifier defined in (40)–(41) with $\gamma \ll \frac{\Delta x}{3}$. Further, the initial macroscopic conditions for the enzymatic components entering the uPA system are considered as follows:

$$\begin{aligned} u(x,0) &= 1 - \frac{1}{2}c(x,0), \qquad x \in Y \\ p(x,0) &= \frac{1}{2}c(x,0), \qquad x \in Y \\ m(x,0) &= \frac{1}{20}c(x,0), \qquad x \in Y \end{aligned} \tag{20}$$

At the same time, in all the subsequent simulations, we consider the following homogeneous and heterogeneous initial condition for ECM, namely,

$$\begin{aligned} &\text{homogeneous case: } v(x,0) = 1 - c(x,0), && x \in Y, \\ &\text{heterogeneous case: } v(x,0) = \frac{1 + 0.3\sin(4\pi||x||_2) + \sin(4\pi||(4,0) - x||_2)}{2}, && x \in Y. \end{aligned} \tag{21}$$

Figure 1 shows the initial conditions (19) and (21) of ECM and cancer cell distributions for both homogeneous and heterogeneous cases that are used in all the simulations presented in this paper.

Finally, in the absence of medical data, for the tissue threshold $\omega(\beta, \epsilon Y)$ controlling whether or not a point on the boundary will exercised the movement according to the direction and displacement magnitude defined in "The multiscale moving boundary approach for the proposed cancer invasion model" section of "Appendix 1", we adopt the following functional form:

$$\omega(\beta, \epsilon Y) := \begin{cases} \sin\left(\frac{\pi}{2}\left(1 - \frac{1}{\beta}\frac{v_{\omega(t_0)}(x^*_{\epsilon Y}, t_0+\Delta t)}{\sup\limits_{\xi \in \partial\Omega(t_0)} v_{\Omega(t_0)}(\xi, t_0+\Delta t)}\right)\right) & \text{if } \frac{v_{\omega(t_0)}(x^*_{\epsilon Y}, t_0+\Delta t)}{\sup\limits_{\xi \in \partial\Omega(t_0)} v_{\Omega(t_0)}(\xi, t_0+\Delta t)} \leq \beta \\ \sin\left(\frac{\pi}{2(1-\beta)}\left(\frac{v_{\omega(t_0)}(x^*_{\epsilon Y}, t_0+\Delta t)}{\sup\limits_{\xi \in \partial\Omega(t_0)} v_{\Omega(t_0)}(\xi, t_0+\Delta t)} - \beta\right)\right) & \text{if } \frac{v_{\omega(t_0)}(x^*_{\epsilon Y}, t_0+\Delta t)}{\sup\limits_{\xi \in \partial\Omega(t_0)} v_{\Omega(t_0)}(\xi, t_0+\Delta t)} > \beta \end{cases} \tag{22}$$

where $\beta \in (0, 1)$ is a parameter that controls a certain "optimal level" of ECM degradation and consider this as being the indicator of the most favourable invasion conditions at the level of tumour and tissue microenvironment. This functional form of ω rules out any invasion if either a complete destruction or a very superficial degradation of the surrounding ECM is performed by the MDEs. This is due to the fact that while for invasion the cancer cells need considerable level of the ECM degradation, a total destruction of the surrounding ECM structure prevents them to advance further into the tissue, as they need some of the ECM components to adhere to in order to migrate. Finally, while this functional form of the tissue threshold aimed to showcase the proposed multiscale modelling framework, future work seeks to infer $\omega(\cdot, \epsilon Y)$ from medical imaging data of the peritumoural tissue.

The following figures show the simulation results of the evolving cancer cell and ECM spatial distributions and of the invasive tumour boundary at macrotime stage

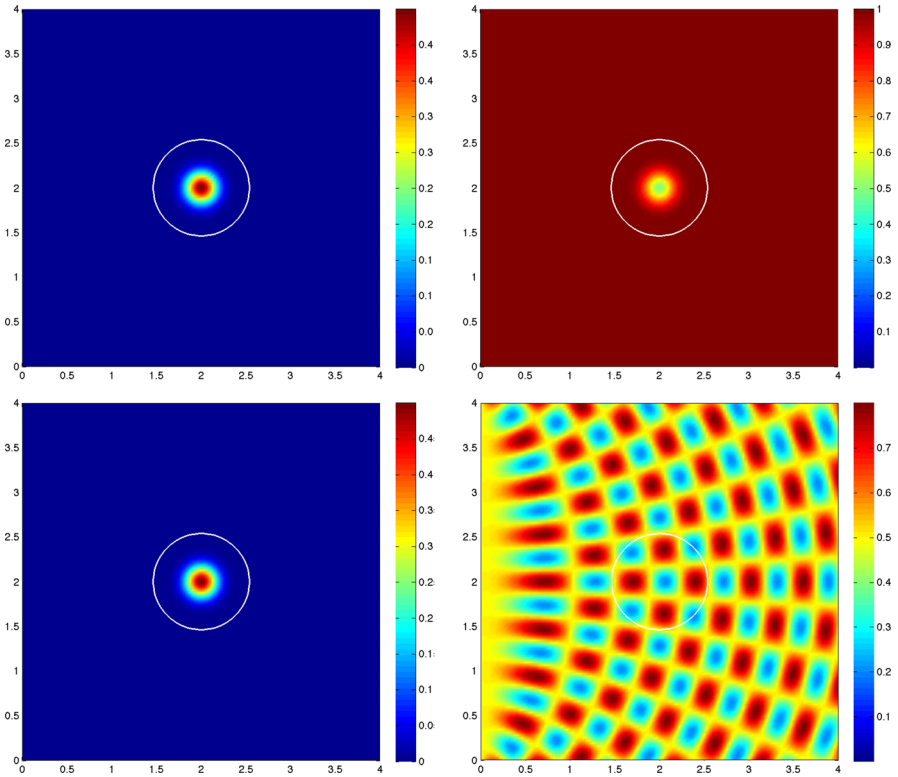

Fig. 1 Initial conditions of the distributions of cancer cells (*left column*) and ECM (*right column*) and the invasive boundary of the tumour (*white line*) for the homogeneous case (*top row*) and the heterogeneous case (*bottom row*) (Color figure online)

20, 40, 60. The images are presented in two columns, with the left columns representing the cancer cell distribution and right columns showing the corresponding ECM concentrations. Furthermore, all these images include the tumour boundary.

In the subsequent simulations, for the macroscopic part of the model, except otherwise stated, we will generally be using the following basic set of parameter values $\mathscr{P}$:

$$
\begin{aligned}
&D_n = 4.3\times10^{-3}, && \chi_u = 3.05\times10^{-2}, && \chi_p = 3.75\times10^{-2}, && \chi_v = 2.85\times10^{-2},\\
&\mu_1 = 0.25, && \delta = 1.5, && \phi_{21} = 0.75, && \phi_{22} = 0.55,\\
&\mu_2 = 0.15, && D_u = 2.5\times10^{-3}, && \phi_{31} = 0.75, && \phi_{33} = 0.3,\\
&\alpha_{31} = 0.215, && D_p = 3.5\times10^{-3}, && \phi_{41} = 0.75, && \phi_{42} = 0.55,\\
&\alpha_{41} = 0.5, && D_m = 4.91\times10^{-3}, && \phi_{52} = 0.11, && \phi_{53} = 0.75,\\
&\phi_{54} = 0.5, && && && && (23)
\end{aligned}
$$

which are detailed in Table 1 in "Table for the parameter Set $\mathscr{P}$" section of "Appendix 3". However, in order to investigate different cancer growth patterns, as described in

the following simulation, we will perform numerical tests also for slightly changed values for the diffusion coefficient of cancer cells D_c, the ECM proliferation rate μ_2 or the ECM degradation rate δ. Also, we will explore a range of values for parameter β, to highlight the correlation between changes in tissue microenvironment conditions and the resulting cancer invasion patterns.

In order to analyse the effect of each variables (namely ECM initial condition, cancer cell diffusion coefficient, ECM proliferation and degradation rates, and threshold coefficient), we will split the results into four groups as follows:

4.1 ECM Initial Condition

To investigate what effect do different ECM initial conditions have on the whole dynamics of the model, we apply the same threshold function for both homogeneous and heterogeneous ECM scenario.

The ECM heterogeneity gives rise to a tumour–tissue interaction that is naturally more complex than in the case of homogeneous ECM. A direct consequence of this is that the ECM heterogeneity triggers a corresponding intrinsic variability in the tissue thresholds, which explore the peritumoural tissue conditions that the cancer interacts with during invasion. This results in a higher degree of complexity in the spatial structure of the regions with most favourable conditions for the tumour to progress further in the surrounding region, within the directions and displacement magnitudes specified by the microscale dynamics. Ultimately, this gives rise to a higher level of fingering and infiltrative patterns in the heterogeneous case as opposed to the homogeneous case. This is confirmed by our results presented in Fig. 3 that are obtained for the heterogeneous ECM, which exhibit more "fingered" and infiltrative spreading of the tumour compared with those obtained in the homogeneous ECM case shown in Fig. 2. This type of fingering patterns is often observed in medical imaging data, such as the one reported in the case of oesophageal and lung cancer by the authors in Ito et al. (2012) and Masuda et al. (2012), respectively.

4.2 Cancer Cell Diffusion Coefficient D_c

As was demonstrated in Hillen et al. (2013) and Painter and Hillen (2011), the chemotaxis terms in the cancer cell Eq. (6) are the main causes of the occurrence of heterogeneous patterns inside the tumour domain. Therefore, if the cancer cell diffusion coefficient (D_c) is increased to be one order magnitude larger than the chemotaxis coefficients (χ_u and χ_p), which becomes the dominant mechanism of cell movement, then no heterogeneous dynamics will occur inside the tumour as shown in Fig. 4. In Fig. 5, the chemotaxis coefficients are one order magnitude larger than the diffusion coefficient, and as a consequence, we obtain heterogeneous pattern formation of cancer cells, which leads to a more dynamic tumour boundary deformation.

4.3 ECM Proliferation Rate μ_2 and Degradation Rate δ

From all the simulation results presented so far, we conclude that the degradation of ECM facilitates cancer invasion. However, as shown also in several interdisciplinary

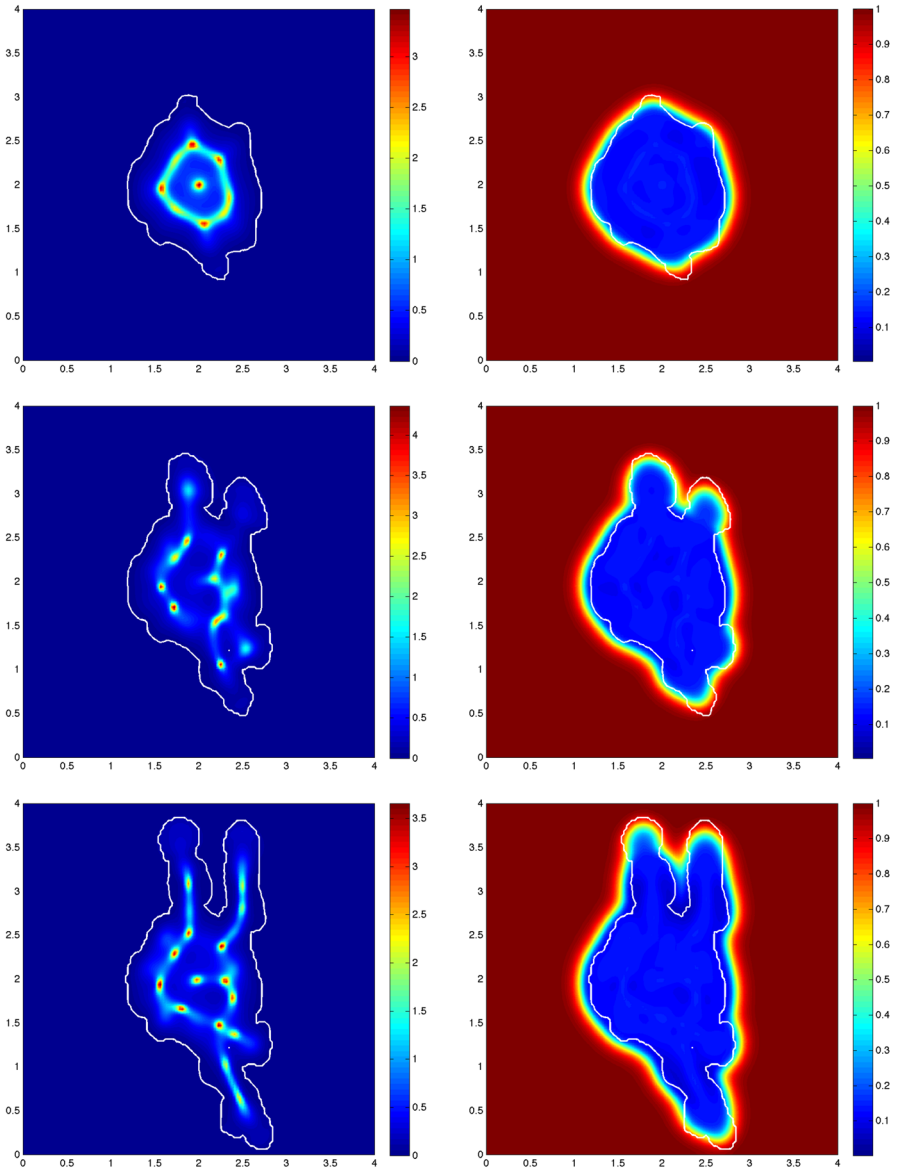

Fig. 2 Simulation results showing distributions of cancer cells (*left column*) and ECM (*right column*) and the invasive boundary of the tumour (*white line*) at various macro-micro stages: stage 20, 40, 60. Starting from the homogeneous initial conditions shown in Fig. 1, these results were obtained for $D_c = 4.3 \times 10^{-3}$, $\beta = 0.775$, $\mu_2 = 0.01$ and $\delta = 1.5$ (Color figure online)

biological investigations (Gatenby and Gawlinski 1996; Gatenby et al. 2006; Stetler-Stevenson et al. 1993), the invasion process will stop where ECM is degraded a lot. This captures the biological scenario in 2D that when cell-matrix adhesion is too low, no focal adhesions or stress fibres are formed, and the cells do not move. In

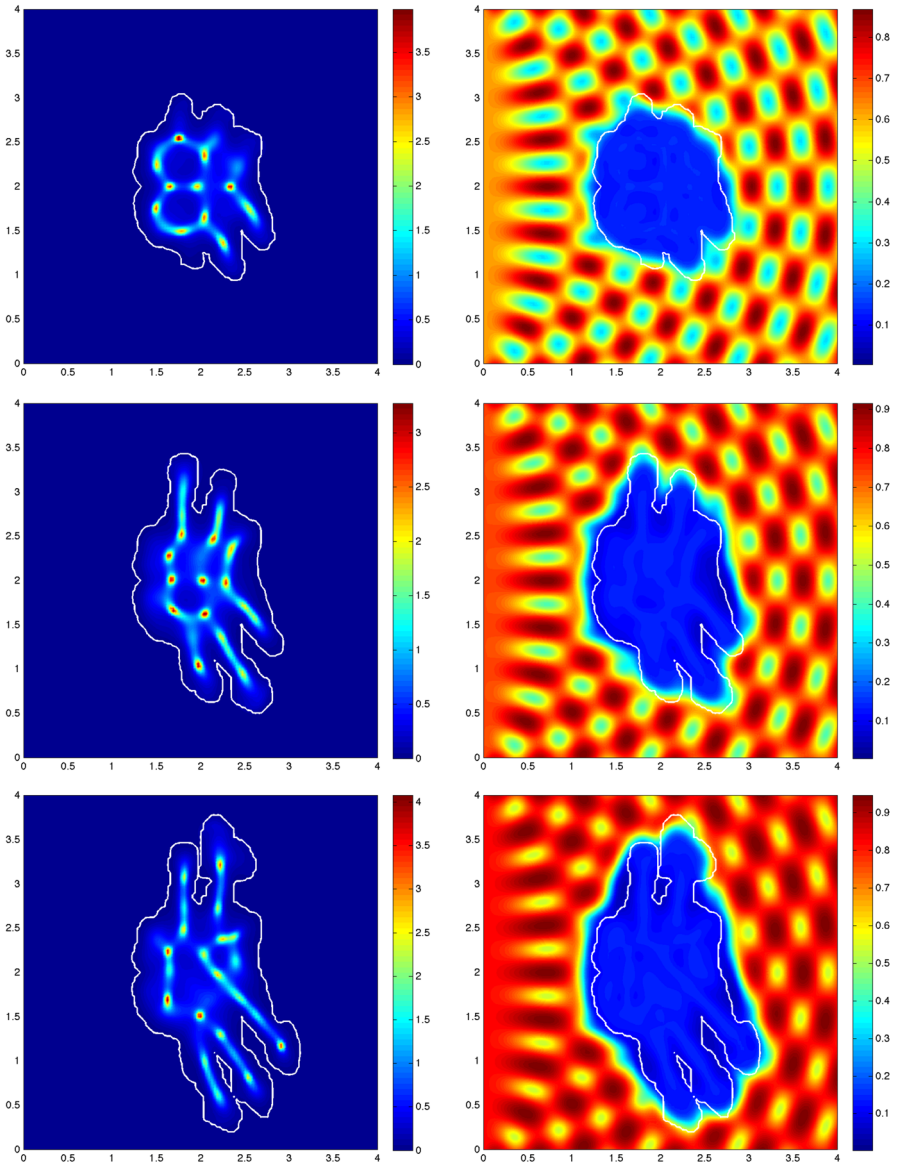

Fig. 3 Simulation results showing distributions of cancer cells (*left column*) and ECM (*right column*) and the invasive boundary of the tumour (*white line*) at various macro-micro stages: stage 20, 40, 60. Starting from the heterogeneous initial conditions shown in Fig. 1, these results were obtained for $D_c = 4.3 \times 10^{-3}$, $\beta = 0.775$, $\mu_2 = 0.01$ and $\delta = 1.5$ (Color figure online)

order to investigate the effect of ECM proliferation and degradation on the invasion process, we compare two groups of parameters: (1) $\mu_2 = 0.01$, $\delta = 1.5$ (nonzero proliferation rate with relatively large degradation rate, Fig. 6); (2) $\mu_2 = 0$, $\delta = 0.75$ (no proliferation with relatively small degradation rate, Fig. 7). From these two groups

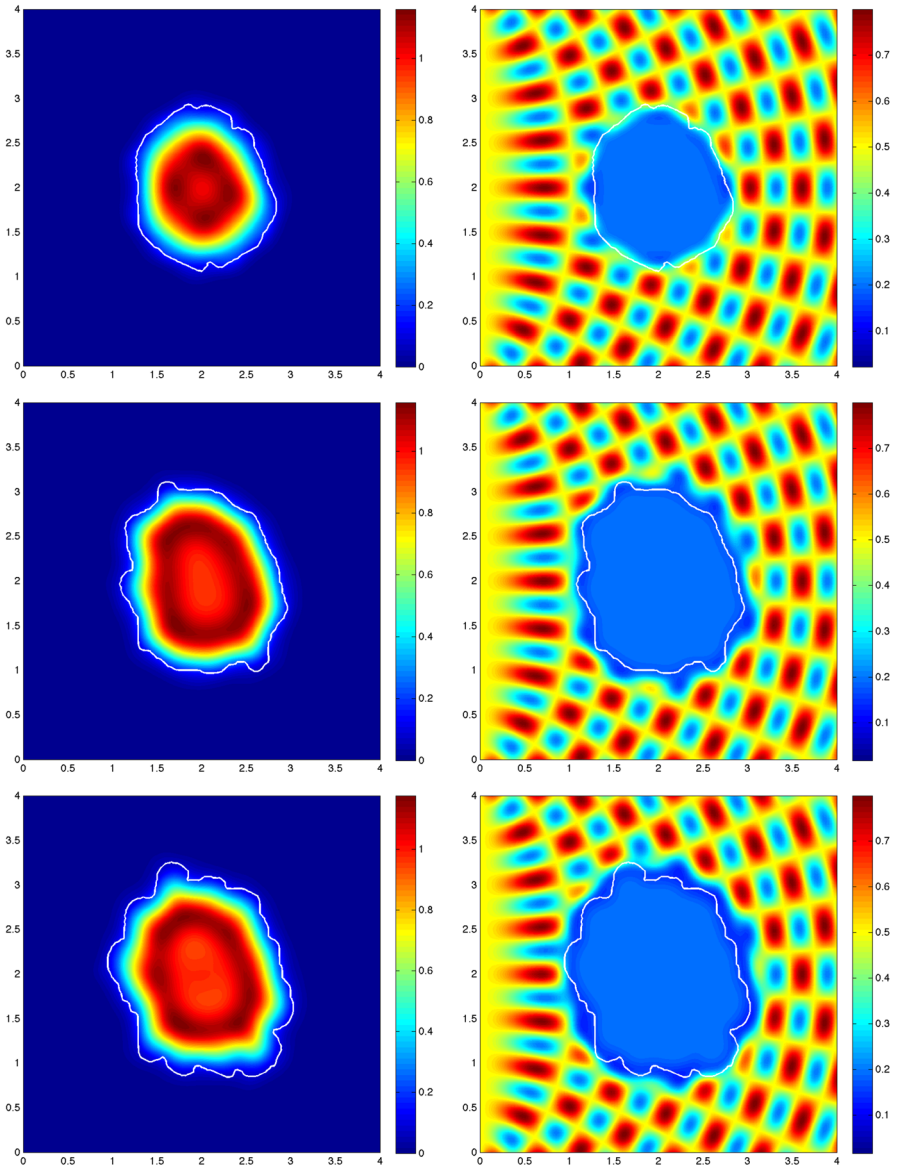

Fig. 4 Simulation results showing distributions of cancer cells (*left column*) and ECM (*right column*) and the invasive boundary of the tumour (*white line*) at various macro-micro stages: stage 20, 40, 60. Starting from the heterogeneous initial conditions shown in Fig. 1, these results were obtained for $D_c = 1.4 \times 10^{-2}$, $\beta = 0.775$, $\mu_2 = 0$ and $\delta = 0.75$ (Color figure online)

of images, we observe that when proliferation is present and the degradation rate is relatively large, deformations of the boundary are not as dynamic as that when the proliferation term is absent with a relatively small degradation rate. The reason could be that the proliferation term will reduce the degree of heterogeneity of the distribution of ECM, which leads to a less fingered spreading of the cancer cell population.

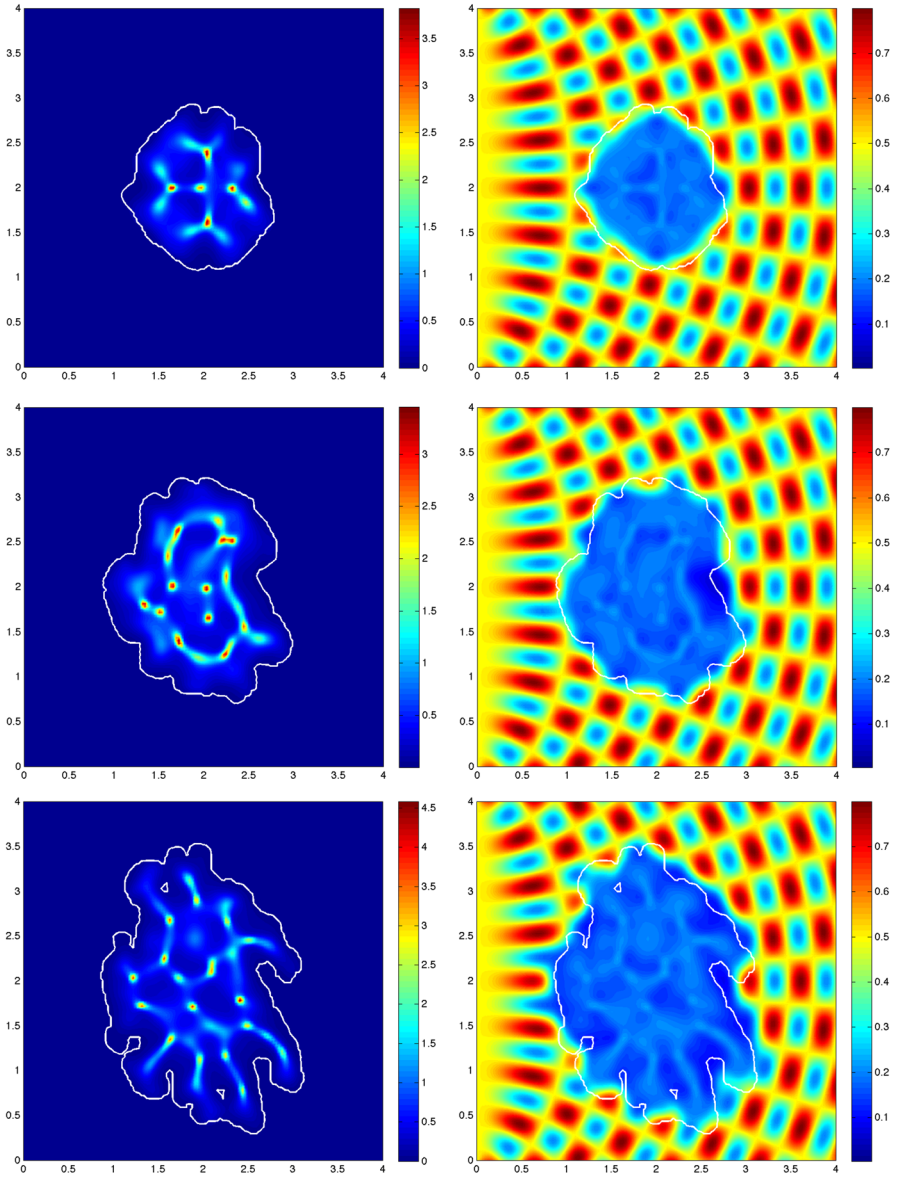

Fig. 5 Simulation results showing distributions of cancer cells (*left column*) and ECM (*right column*) and the invasive boundary of the tumour (*white line*) at various macro-micro stages: stage 20, 40, 60. Starting from the heterogeneous initial conditions shown in Fig. 1, these results were obtained for $D_c = 4.3 \times 10^{-3}$, $\beta = 0.775$, $\mu_2 = 0$ and $\delta = 0.75$ (Color figure online)

Figure 8 shows the results of simulations at the macro-micro stage 60 where the ECM proliferation rate parameter μ_2 was increased over a range of values in the interval $[0.0005, 0.005]$. The figures show that, over the range chosen, there is little

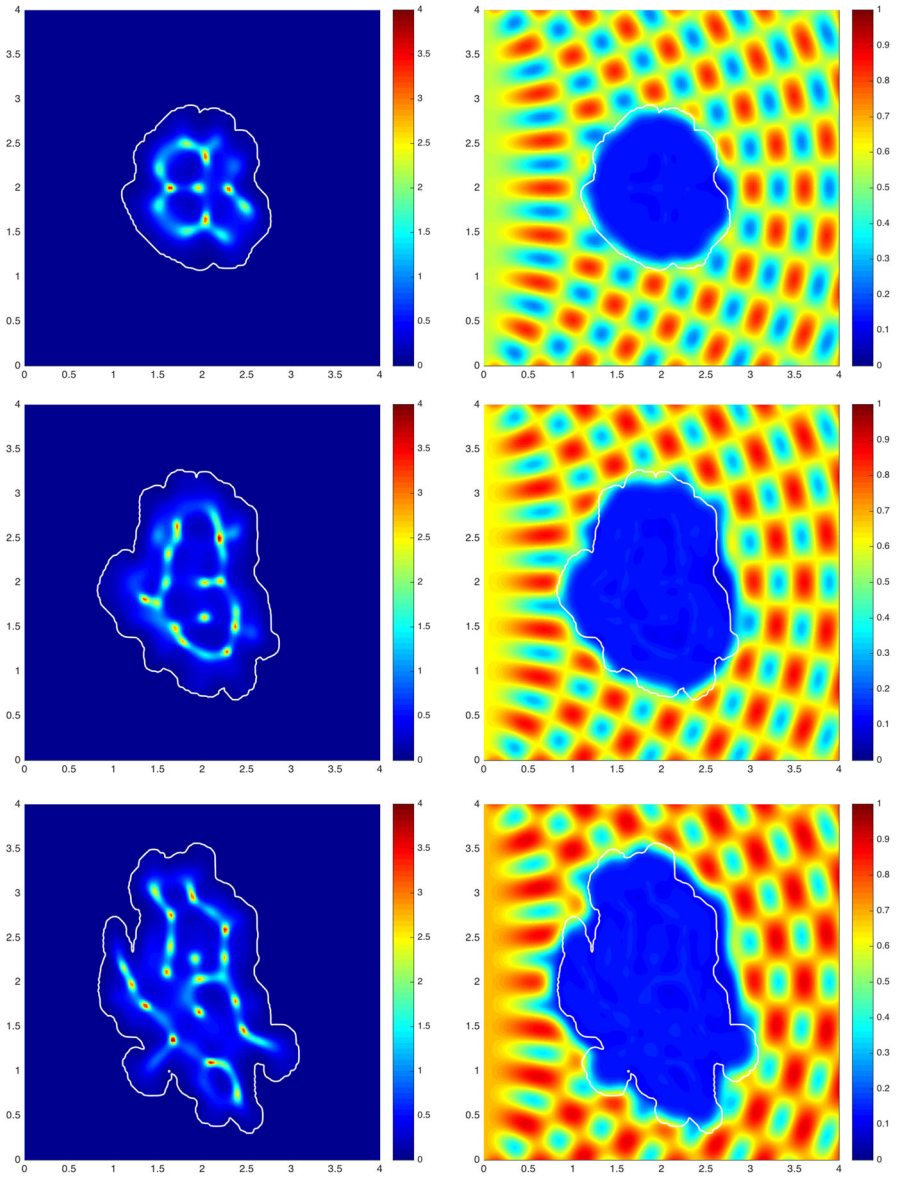

Fig. 6 Simulation results showing distributions of cancer cells (*left column*) and ECM (*right column*) and the invasive boundary of the tumour (*white line*) at various macro-micro stages: stage 20, 40, 60. Starting from the heterogeneous initial conditions shown in Fig. 1, these results were obtained for $D_c = 4.3 \times 10^{-3}$, $\beta = 0.7625$, $\mu_2 = 0.005$ and $\delta = 1.5$ (Color figure online)

difference in either the overall extent of invasion or the morphology of the invading cancer. Figure 9 shows the results of simulations at the same macro-micro stage 60 where the degradation parameter δ was increased over the interval [0.5, 1]. The figures show that, over the range chosen, the extent of the invasion is similar, but the

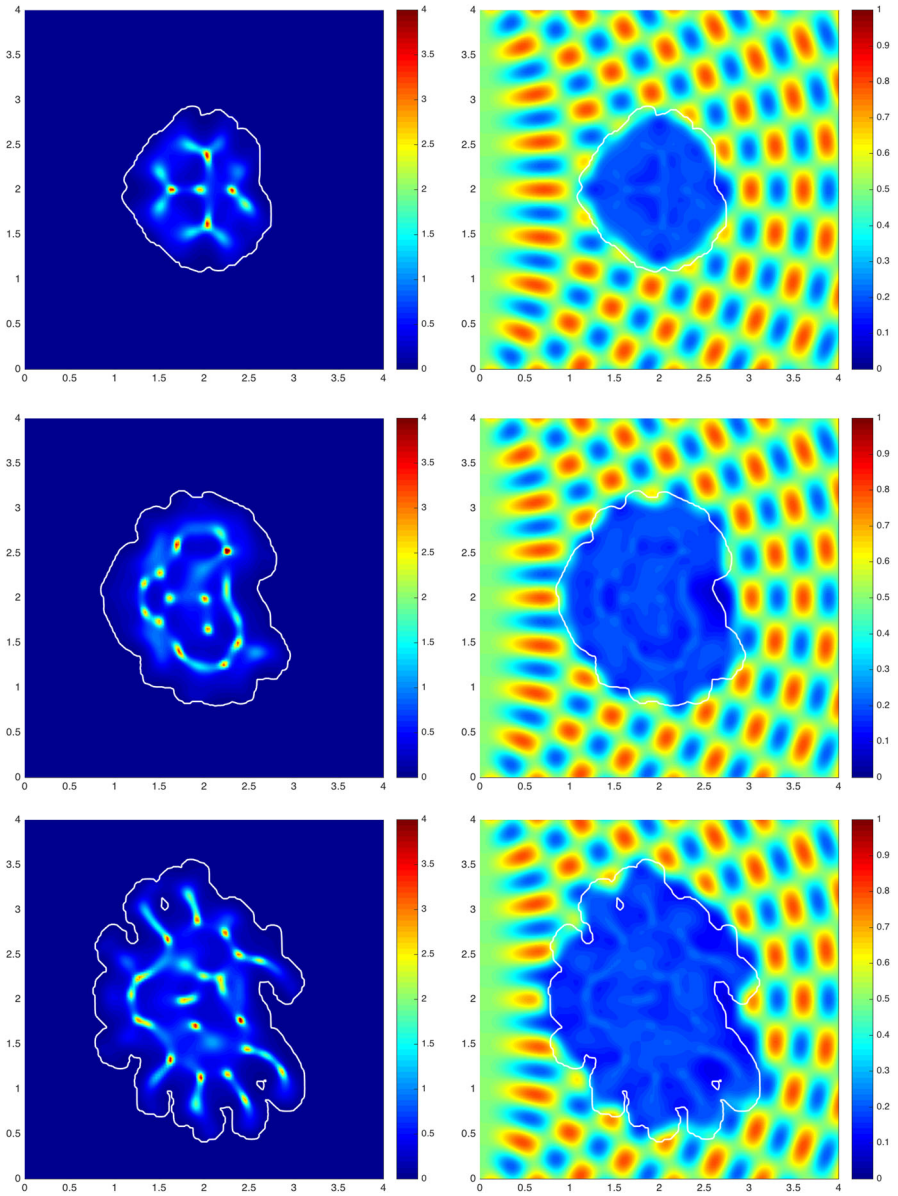

Fig. 7 Simulation results showing distributions of cancer cells (*left column*) and ECM (*right column*) and the invasive boundary of the tumour (*white line*) at various macro-micro stages: stage 20, 40, 60. Starting from the heterogeneous initial conditions shown in Fig. 1, these results were obtained for $D_c = 4.3 \times 10^{-5}$, $\beta = 0.7625$, $\mu_2 = 0$ and $\delta = 0.75$ (Color figure online)

morphology of the invading cancer changes slightly from a more fingered boundary to a less fingered boundary. Finally, as the two parameters μ_2 and δ are varied, both Figs. 8 and 9 exhibit spatial consistency aspects in the invasion pattern.

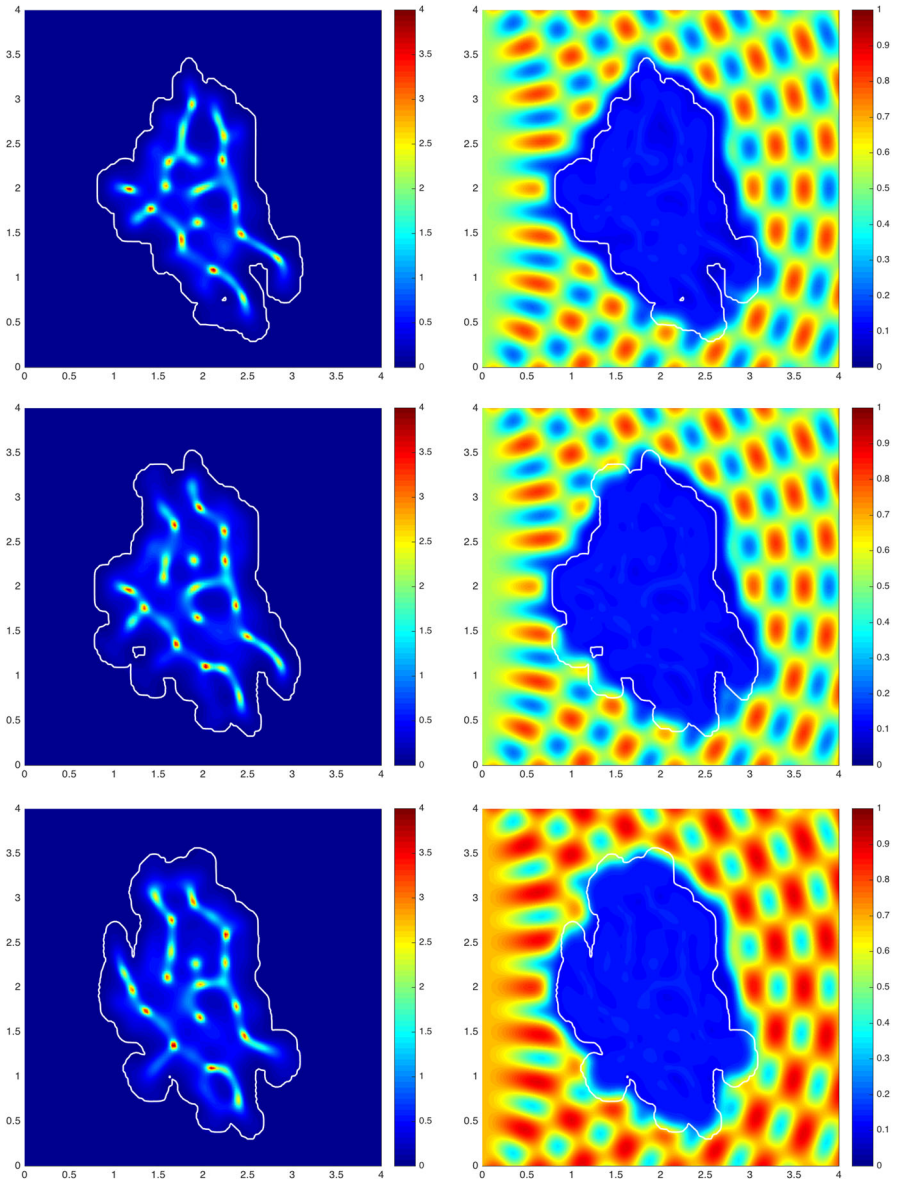

Fig. 8 Simulation results showing distributions of cancer cells (*left column*) and ECM (*right column*) and the invasive boundary of the tumour (*white line*) at macro-micro stage 60. Starting from the heterogeneous initial conditions shown in Fig. 1, these results were obtained for $D_c = 4.3 \times 10^{-3}$, $\beta = 0.7625$, $\delta = 1.5$, and for rows 1 to 3 of images we consider $\mu_2 = 0.0005$, $\mu_2 = 0.001$, and $\mu_2 = 0.005$, respectively (Color figure online)

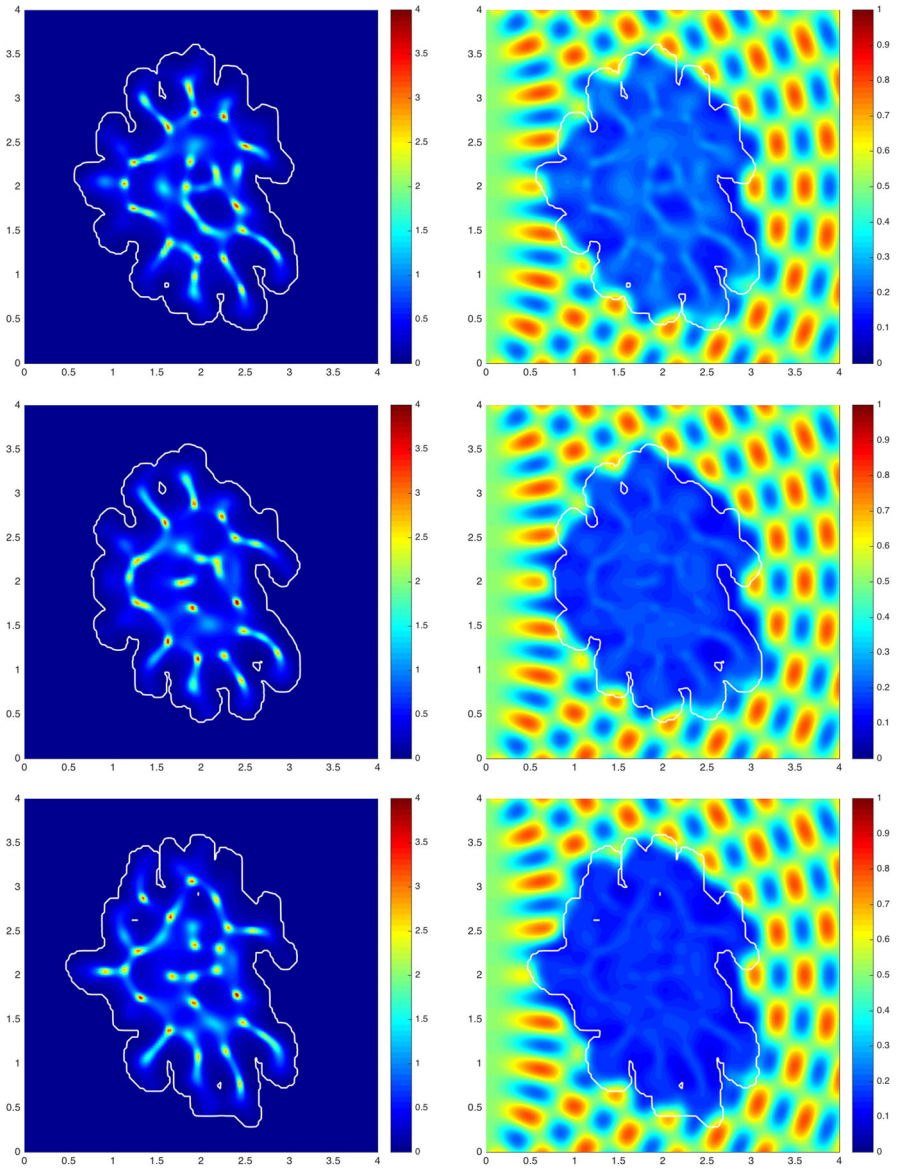

Fig. 9 Simulation results showing distributions of cancer cells (*left column*) and ECM (*right column*) and the invasive boundary of the tumour (*white line*) at macro-micro stage 60. Starting from the heterogeneous initial conditions shown in Fig. 1, these results were obtained for $D_c = 4.3 \times 10^{-3}$, $\mu_2 = 0$, $\beta = 0.7625$, and for rows 1 to images we consider $\delta = 0.5$, $\delta = 0.75$, and $\delta = 1$, respectively (Color figure online)

4.4 Threshold Coefficient β

Finally, Fig. 10 shows us comparative results at macro-micro stage 60 for several values of the threshold coefficients β in the interval $[0.7625, 0.7875]$. Since β controls the "optimal level" of ECM density for cancer cells to migrate, its variation gives

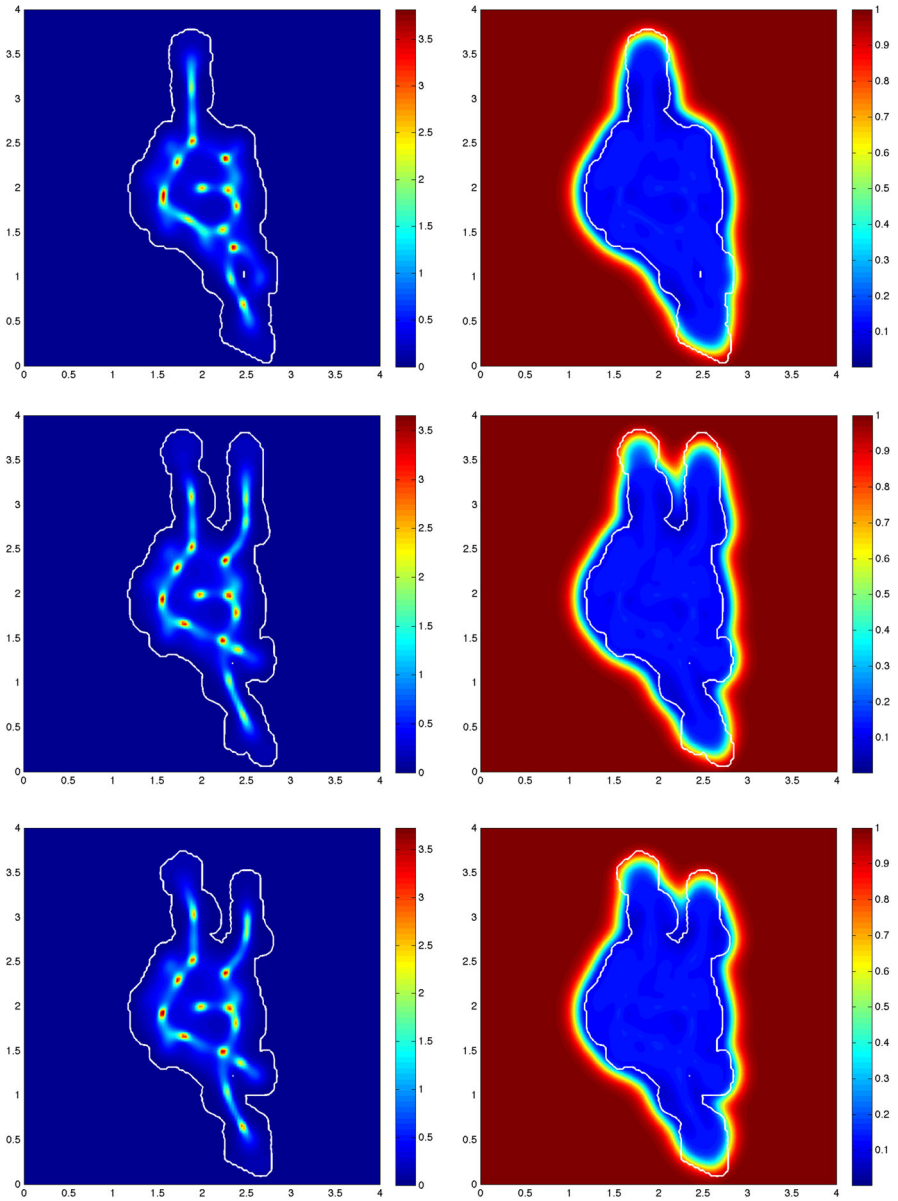

Fig. 10 Simulation results showing distributions of cancer cells (*left column*) and ECM (*right column*) and the invasive boundary of the tumour (white line) at macro-micro stage 60. Starting from the homogeneous initial conditions shown in Fig. 1, these results were obtained for $D_c = 4.3 \times 10^{-3}$, $\delta = 1.5$, $\mu_2 = 0.01$, and for rows 1 to 3 of images we consider $\beta = 0.7625$, $\beta = 0.775$, and $\beta = 0.7875$, respectively (Color figure online)

us different invasion morphologies, as expected. Again, as we noticed also in the cases of Figs. 8 and 9, a quick comparison between consecutive rows of images (from top to bottom) in Fig. 10 seems to indicate a certain degree of consistency in the

changes occurring in the tumour morphology and "fingered" boundary deformations with respect to increasing β parameter. This consistency aspect is currently under investigation and will form the topic of a separate research work.

5 Conclusion

In this paper, we presented and developed a mathematical model of cancer invasion based on the previous work in Andasari et al. (2011), Chaplain and Lolas (2005) and Trucu et al. (2013). We adapted and extended the two-scale technique in Trucu et al. (2013) to cope with the different settings that enable the coupling of the finite difference uPA macrosolver and a new finite element microsolver developed for the newly proposed leading edge microdynamics. This enabled us to simulate the multiscale process of cancer invasion by exploring the link between the macroscopic dynamics of the spatio-temporal distribution of cancer cells and ECM taking place on a macroscopic domain, and the matrix degrading enzymes microdynamics developed on the microscopic domains that are in close proximity to tumour boundary.

We derived a new governing law for the microdynamics based exclusively on the molecular mechanics of the uPA system occurring in close proximity to the tumour boundary. This is based on the dynamics of the uPA system including uPA, the inhibitor uPA-1 and plasmin and considers the source terms related to macroscopic components, i.e. cancer cells and ECM molecules, in a collective fashion, and we solve this new microscopic uPA system by finite element method. While this is sourced from within the macrodynamics via a top-down link, in our multiscale method (described in "The multiscale moving boundary approach for the proposed cancer invasion model" section of "Appendix 1") the microdynamics occurring at the cell-scale neighbourhood of the tumour is represented back at the macroscale through a bottom-up feedback by defining the movement direction and displacement magnitude of the tissue-scale tumour boundary. By coupling this new microscopic governing law for the leading edge microdynamics with the macroscopic model for the uPA system and cancer invasion proposed in Andasari et al. (2011) and Chaplain and Lolas (2005), we are able to capture an important class of multiscale dynamic interactions between cancer cells, ECM molecules, cancer associated matrix degrading enzymes and the peritumoural tissue conditions, leading to significant changes in tumour morphology during invasion.

From the computational simulation results of our model, we can see that the extended two-scale technique coupled with the uPA system and more specific modelling of the pericellular proteolytic activities gives more adverse dynamics in the invading cancer. Values of the ECM initial condition, the cancer cell diffusion coefficient, the threshold coefficient, and the ECM proliferation and degradation rates all have an impact on the deformations of the tumour boundary. While for simulating the proposed non-dimensional model we considered functional formulations for the initial conditions and tissue thresholds, future work will attempt to assimilate the heterogeneity of ECM and as well as the peritumoural tissue conditions from imaging data. Finally, concerning the transitional probability that arises naturally at the microscale and intervenes in the bottom-up link between micro- and macroscales,

while the simulations presented in this paper are deterministic, future work will assess the stochastic character of the overall model.

The conclusions that can be drawn from the qualitative results presented in this paper are: (1) a heterogeneous ECM initial condition leads to more fingered spreading of the tumour compared with that in the homogeneous ECM; (2) in order to obtain heterogeneous patterns of cancer cells inside the tumour region, chemotaxis must be dominant to drive the cells migration; (3) the changes of threshold coefficient will definitely affect the boundary deformations, and there is a tendency that the increase in β reduces the number of 'fingers' of the interface; and (4) without a proliferation term of ECM coupled with a relatively small degradation rate, deformations of the boundary show more fingering. However, further investigations are required to analyse the observed fingering. For instance, the dependence of the width of the fingers on the size of the microscale and potentially on other regulatory parameters remains an open question and is an important objective of a future work on the propose modelling framework.

It is useful to compare these results with other models of cancer growth and invasion, particularly those that adopt an alternative modelling approach such as hybrid continuum-discrete, cellular-Potts or cellular automaton, as well as partial differential equations (PDE) models. Many PDE models of solid tumour growth and development (including invasion) have modelled cell–cell adhesion at the outer boundary (or invading edge) of the tumour as a surface-tension-like force (Byrne and Chaplain 1996, 1997). A reduction in surface tension, i.e. interpreted as a loss of cell–cell adhesion, then leads to an instability at the invading edge which manifests itself in a subsequent growth consisting of finger-like protrusions. This effect was shown computationally by Cristini et al. (2003) and Macklin and Lowengrub (2007) who demonstrated a range of fingering patterns as a cell adhesion parameter was varied. Similar spectra of invasive patterns have been observed when adopting either a cellular-Potts approach (Popławski et al. 2009) or a hybrid continuum-discrete approach (Anderson 2005), i.e. by varying a key cell–cell adhesion parameter of the model, invasive fingering patterns can either be enhanced or suppressed. In the specific case of glioma invasion, four different approaches—PDE, cellular-Potts, lattice-gas automaton, cellular automaton—have each investigated the role of cell–cell adhesion and compared computational simulation results with experimental data (Aubert et al. 2006; Frieboes et al. 2007; Rubenstein and Kaufman 2008; Tektonidis et al. 2011. Given these results, we are currently extending our current model to include cell–cell adhesion.

As the main purpose of this work was to formulate a novel non-dimensional two-scale modelling platform that simultaneously explores spatio-temporal dynamics at both macroscale (cell population level) and microscale alongside the links in between the two scales, the simulations presented here have a qualitative character. Future work will explore the possibilities of dimensionalising and calibrating the proposed multi-scale model with measured data at both macroscopic (tissue-scale) and microscopic (cell-scale) levels to obtain quantitative simulation that we could compare with clinical observations.

The two-scale modelling described provides a useful mathematical platform to capture and investigate processes at different levels during cancer invasion. However, further details remain to be explained on the dynamics and interactions of the tumour

cell community at the macrolevel and the microlevel as well as regarding the links in between these two scales. Various avenues could be pursued to extend our modelling by exploring for instance other ways to determine the cancer cell population macrodynamics (for example change the definition of the threshold function ω characterising the interaction with the peritumoural tissue) or by accounting for more complex signalling mechanisms in the establishment of more detailed microdynamics as well as the appropriate top-down and bottom-up links between these different levels (scales) of the invasion process.

Appendix 1: The Two-Scale Computational Modelling Method

In the following, we will briefly present the technique introduced in Trucu et al. (2013) and adjust this with all the details to our new situation. For completion, we introduce here all the necessary notations and describe the defining principles that are referred to in the paper, as well as the relevant considerations and explanations concerning our new model.

Preliminary Considerations and Notations

It is assumed that the domain within which the cancer and extracellular matrix exist is a maximal reference spatial cube $Y \subset \mathbb{R}^n (n = 2, 3)$ with its centre at the origin. Given a fixed ϵ representing a negative power of 2 (i.e. $0 < \epsilon < 1$), the initial Y is uniformly decomposed ϵ-size cubes, ϵY, whose union will be referred to as an ϵ-resolution of Y. For any ϵY from the decomposition, the "half-way shifted" cubes in the direction $i\bar{e}_1 + j\bar{e}_2 + k\bar{e}_3$ given by any triplet $(i, j, k) \in \{(i, j, k)|i, j, k \in \{-1, 0, 1\}\}$ are defined as

$$\epsilon Y_{\frac{i}{2},\frac{j}{2},\frac{k}{2}} = \epsilon Y + \frac{\epsilon(i\bar{e}_1 + j\bar{e}_2 + k\bar{e}_3)}{2}, \tag{24}$$

where,

$$\bar{e}_1 := e_1, \qquad \bar{e}_2 := e_2, \qquad \text{and,} \qquad \bar{e}_3 := \begin{cases} e_3 \text{ for } & N = 3, \\ 0 \text{ for } & N = 2, \end{cases} \tag{25}$$

and $\{e_1, e_2, e_3\}$ is the standard Euclidean basis of $\mathbb{R}^3$. The family of all these $\epsilon-$cubes is denoted by $\mathcal{F}$, i.e.

$$\mathcal{F} := \bigcup_{i,j,k\in\{-1,0,1\}} \left\{ \epsilon Y_{\frac{i}{2},\frac{j}{2},\frac{k}{2}} \middle| \epsilon Y \text{ is in the } \epsilon\text{-resolution of } Y \right\}. \tag{26}$$

In Fig. 11, the notations mentioned so far are illustrated schematically.

In order to capture mathematically the microdynamics that occur in a cell-scale neighbourhood of the tumour boundary $\partial\Omega(t_0)$, out of the initial family $\mathcal{F}$, we will focus our attention of the subfamily denoted by $\mathcal{F}_{\Omega(t_0)}$ which consists of only the $\epsilon-$cubes that cross the interface $\partial\Omega(t_0)$ and have exactly one face included in the

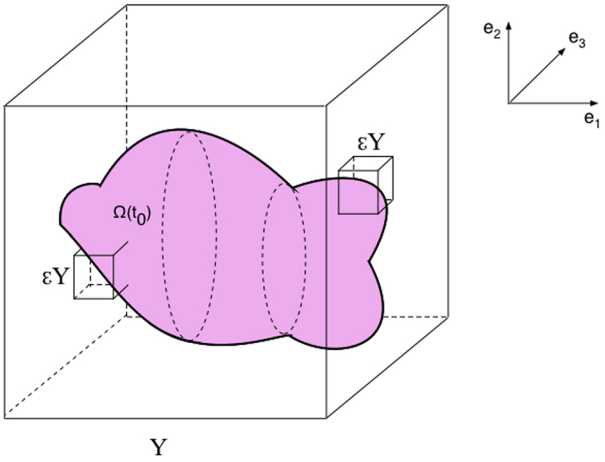

Fig. 11 Schematic diagram showing the cubic region Y centred at the origin $\in \mathbb{R}^3$. The *dashed blue lines* represent the Euclidean directions $\{e_1, e_2, e_3\}$, the *pink region* illustrates the cancer cluster $\Omega(t_0)$, and the *solid blue line* represents the family of microscopic cubic domains ϵY placed at the boundary $\partial\Omega(t_0)$ (Color figure online)

interior of $\Omega(t_0)$, namely

$$\mathcal{F}_{\Omega(t_0)} := \{\epsilon Y \in \mathcal{F} | \epsilon Y \cap (Y \backslash \Omega(t_0)) \neq \emptyset, \\ \text{and } \epsilon Y \text{ has only one face included in int}(\Omega(t_0))\}, \tag{27}$$

where $\text{int}(\Omega(t_0))$ is the topological interior of $\Omega(t_0)$ with respect to the natural topology on $\mathbb{R}^n$.
In this context, for each $\epsilon Y \in \mathcal{F}_{\Omega(t_0)}$, we have the following face notations:

$$\begin{cases} \Gamma_{\epsilon Y}^{\text{int}} \text{ denotes the face of } \epsilon Y \text{ that is included in int}(\Omega(t_0)), \\ \Gamma_{\epsilon Y}^{j,\perp},\ j = 1, ..., 2^{N-1} \text{ denote the faces of } \epsilon Y \text{ that are perpendicular to } \Gamma_{\epsilon Y}^{\text{int}} \\ \Gamma_{\epsilon Y}^{\parallel} \text{ denotes the face of } \epsilon Y \text{ that is parallel to } \Gamma_{\epsilon Y}^{\text{int}}. \end{cases} \tag{28}$$

These are illustrated schematically in Fig. 12.

Furthermore, for each $\epsilon Y \in \mathcal{F}_{\Omega(t_0)}$, the topological closure of the only connected component of $\Omega(t_0) \cap \epsilon Y$ that is confined between $[\partial\Omega(t_0)]_{\epsilon Y}$ and $\Gamma_{\epsilon Y}^{\text{int}}$ is denoted by $[\Omega(t_0)]_{\epsilon Y}$. Moreover, denoting by $[\partial\Omega(t_0)]_{\epsilon Y}$ the connected component part of $\partial\Omega(t_0) \cap \epsilon Y$ with the property that

$$[\partial\Omega(t_0)]_{\epsilon Y} \cap \Gamma_{\epsilon Y}^{j,\perp} \neq \emptyset \qquad \text{for any } j = 1, 2, ..., 2^{n-1}, \tag{29}$$

we can observe that $[\partial\Omega(t_0)]_{\epsilon Y}$ represents the part of $\partial\Omega(t_0) \cap \epsilon Y$ that corresponds to $[\Omega(t_0)]_{\epsilon Y}$, and is actually the only connected component of this intersection that has

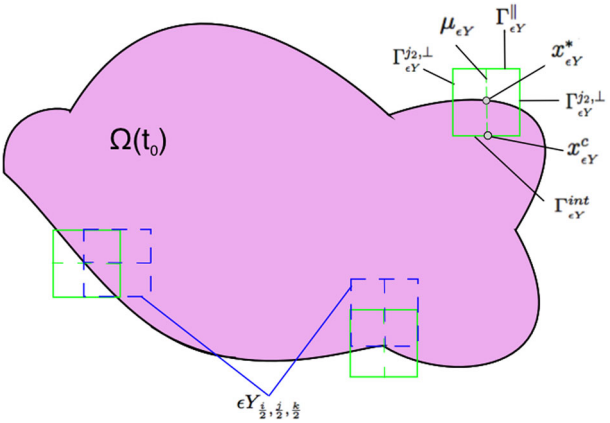

Fig. 12 Schematic diagram illustrating the notations introduced in (28), (32). For the arbitrary microdomain $\epsilon Y \in \mathcal{P}_\epsilon$, we indicate with a *black arrow* the features: $\Gamma^{int}_{\epsilon Y}$, $\Gamma^{j_1,\perp}_{\epsilon Y}$, and $\Gamma^{j_2,\perp}_{\epsilon Y}$, $j_1, j_2 \in \{1, ..., 2^{N-1}\}$, $\Gamma^{\parallel}_{\epsilon Y}$, $x^{c}_{\epsilon Y}$, $\mu_{\epsilon Y}$, and $x^{*}_{\epsilon Y}$. The arbitrary cube $\epsilon Y \in \mathcal{P}^{*}_{\epsilon}$ is shown in *green*, while the corresponding half-way shifted $\epsilon Y^{sign}_{\frac{i}{2}} \in \mathcal{P}_\epsilon$ that are not chosen in $\mathcal{P}^{*}_{\epsilon}$ are shown in the *blue dashed line* (Color figure online)

property (29). Finally, using this observation, for the currently fixed ϵ, the subfamily denoted by $\mathcal{P}_\epsilon$ consisting of all those $\epsilon-$cubes that have $[\Omega(t_0)]_{\epsilon Y}$ not touching $\Gamma^{\parallel}_{\epsilon Y}$ is selected as follows:

$$\mathcal{P}_\epsilon := \{\epsilon Y \in \mathcal{F}_{\Omega(t_0)} |\ [\Omega(t_0)]_{\epsilon Y} \subset \epsilon Y \text{ and } [\partial\Omega(t_0)]_{\epsilon Y} \cap \Gamma^{\parallel}_{\epsilon Y} = \emptyset\}. \tag{30}$$

Leaving now ϵ to take all the negative powers of 2, the union

$$\bigcup_{\epsilon \in \{2^{-k}\,|\,k\in\mathbb{N}\}} \mathcal{P}_\epsilon$$

provides an infinite covering of $\partial\Omega(t_0)$. Since $\partial\Omega(t_0)$ is compact, using standard compactness arguments, a finite complete sub-covering of $\partial\Omega(t_0)$ that consist only of small cubes an equal size ϵ^* is denoted by $\mathcal{P}^{*}_{\epsilon}$, i.e.

$$\partial\Omega(t_0) \subset \bigcup_{\epsilon Y \in \mathcal{P}^{*}_{\epsilon}} \epsilon Y. \tag{31}$$

Together with this finite complete covering $\mathcal{P}^{*}_{\epsilon}$ of the tumour interface $\partial\Omega(t_0)$, at each time of the tumour evolution we obtain also the size of the microscale ϵ^* (Trucu et al. 2013). For simplicity, in this paper, the size of the cell-scale ϵ^* will still be denoted by ϵ. Finally, for each $\epsilon Y \in \mathcal{P}^{*}_{\epsilon}$, we distinguish the following topological details:

$$\begin{cases} x^c_{\epsilon Y} \text{ denotes the centre of the face } \Gamma^{\text{int}}_{\epsilon Y}, \\ \mu_{\epsilon Y} \text{ is the line that passes through } x^c_{\epsilon Y} \text{ and is perpendicular on } \Gamma^{\text{int}}_{\epsilon Y} \\ x^*_{\epsilon Y} \in [\partial\Omega(t_0)]_{\epsilon Y} \text{ which will be referred to as the "midpoint" of } [\partial\Omega(t_0)]_{\epsilon Y} \\ \text{represents the point from the intersection } \mu_{\epsilon Y} \cap [\partial\Omega(t_0)]_{\epsilon Y} \text{ that is located} \\ \text{at the smallest distance with respect to } x^c_{\epsilon Y}. \end{cases} \tag{32}$$

The well-posedness of these topological features is discussed in Trucu et al. (2013), and these are illustrated in Fig. 12.

The Multiscale Moving Boundary Approach for the Proposed Cancer Invasion Model

In the following, we will explain how the set of midpoints $\{x^*_{\epsilon Y}\}_{\epsilon Y \in \mathcal{P}^*_\epsilon}$ defined on the boundary of tumour at the current time moves to a set of new spatial positions $\{\widetilde{x^*_{\epsilon Y}}\}_{\epsilon Y \in \mathcal{P}^*_\epsilon}$ to form the new boundary at the very next time, by describing the movement of one such midpoint $x^*_{\epsilon Y} \in [\partial\Omega(t_0)]_{\epsilon Y}$ for any $\epsilon Y \in \mathcal{P}^*_\epsilon$.

Based on biological observations that, on any microdomain ϵY, provided that a sufficient amount of plasmin has been produced across the invading edge and it is the pattern of the front of the advancing spatial distribution of plasmin that characterised ECM degradation, therefore it is assumed that each boundary midpoint $x^*_{\epsilon Y} \in [\partial\Omega(t_0)]_{\epsilon Y}$ will be potentially relocated in a movement direction and by a certain displacement magnitude dictated by the spatial distribution of plasmin obtained via the microprocess on ϵY at the final microtime $\tau_f := \Delta t$, namely $m(\cdot, \tau_f)$. In the following, we explain how the movement direction and displacement magnitude are defined for each $x^*_{\epsilon Y} \in [\partial\Omega(t_0)]_{\epsilon Y}$.

For any given threshold $\delta > 0$ and any fixed $\epsilon Y \in \mathcal{P}^*_\epsilon$, the regularity property of Lebesgue measure (Halmos 1974) is used to select the first dyadic decomposition $\{D_j\}_{j \in \mathcal{J}_\delta}$ of ϵY such that

$$\lambda\left([\epsilon Y \backslash \Omega(t_0)] \setminus \bigcup_{\{j \in \mathcal{J}_\delta \mid D_j \subset \epsilon Y \backslash \Omega(t_0)\}} \mathcal{D}_j \right) \leq \delta. \tag{33}$$

which simply means that $\epsilon Y \backslash \Omega(t_0)$ is approximated with accuracy δ by the union of all the dyadic cubes that this includes. Once this dyadic decomposition is selected, we denote by y_j the barycenters of D_j, for all $j \in \mathcal{J}_\delta$. As discussed in Trucu et al. (2013) for all $\epsilon Y \in \mathcal{P}^*_\epsilon$, this provides a resolution at which we read the further away part of the level set $\frac{1}{\lambda(\epsilon Y \backslash \Omega(t_0))} \int_{\epsilon Y \backslash \Omega(t_0)} m(y, \cdot) \mathrm{d}y$ in the distribution of the advancing degrading enzymes $m(\cdot, \cdot)$ outside $\Omega(t_0)$ in radial direction with respect to the midpoint $x^*_{\epsilon Y}$. Therefore, this enables us to locate dyadic pixels D_l that support the peaks at the tip of the plasmin front with significant contribution in degrading the ECM. Hence, at the

final microscopic time τ_f, the pixels supporting these peaks are therefore selected as

$$\mathcal{I}_\delta := \left\{ l \in \mathcal{J}_\delta \;\middle|\; \begin{array}{l} \exists r \in S^1 \text{ such that, if the index } i \in \mathcal{J}_\delta \text{ has the properties:} \\ 1)\mathcal{D}_i \cap \{x \in \mathbb{R}^n \,|\, x = x^*_{\epsilon Y} + \alpha r, \alpha \in \mathbb{R}\} \neq \emptyset, \\ 2)\mathcal{D}_i \subset \epsilon Y \backslash \Omega(t_0), \\ 3)\frac{1}{\lambda(\mathcal{D}_i)} \int_{\mathcal{D}_i} m(y, \tau_f)\mathrm{d}y \geq \frac{1}{\lambda(\epsilon Y \backslash \Omega(t_0))} \int_{\epsilon Y \backslash \Omega(t_0)} m(y, \tau_f)\mathrm{d}y, \\ \text{then} \\ l = \text{ argmax } \{d(x^*_{\epsilon Y}, y_i) \,|\, i \in \mathcal{J}_\delta \text{ satisfies: 1), 2), and 3)}\} \end{array} \right\}, \quad (34)$$

where $S^1 \subset \mathbb{R}^n$ represents the unit sphere and $d(\cdot, \cdot)$ is the Euclidean distance on $\mathbb{R}^n$. Thus, cumulating the driving ECM degradation forces spanned by each front peak of plasmin given by the dyadic pixels $\mathcal{D}_l$ with $l \in \mathcal{I}_\delta$ in the direction of the position vectors $\overrightarrow{x^*_{\epsilon Y}, y_l}$ and appropriately representing the amount of plasmin that each D_l supports, the revolving direction of movement $\eta_{\epsilon Y}$ for the potential displacement of $x^*_{\epsilon Y}$ is given by:

$$\eta_{\epsilon Y} = x^*_{\epsilon Y} + \nu \sum_{l \in \mathcal{I}_\delta} \left(\int_{\mathcal{D}_l} m(y, \tau_f)\mathrm{d}y \right)(y - x^*_{\epsilon Y}), \nu \in [0, \infty). \quad (35)$$

Further, the displacement magnitude of the point $x^*_{\epsilon Y}$ is defined as:

$$\xi_{\epsilon Y} := \sum_{l \in \mathcal{I}_\delta} \frac{\int_{\mathcal{D}_l} m(y, \tau_f)\mathrm{d}y}{\sum_{l \in \mathcal{I}_\delta} \int_{\mathcal{D}_l} m(y, \tau_f)\mathrm{d}y} \left| \overrightarrow{x^*_{\epsilon Y} y_l} \right|. \quad (36)$$

Finally, as debated in Trucu et al. (2013), although a displacement magnitude and a moving direction are derived for each $x^*_{\epsilon Y}$, this will only exercise the movement if and only if the ECM degradation were of a certain local strength. The strength of ECM degradation within ϵY is explored by the transitional probability

$$q^* : \sum \left(\bigcup_{\epsilon Y \in \mathcal{P}^*_\epsilon} \epsilon Y \right) \to \mathbb{R}_+$$

defined as

$$q^*(G) := \frac{1}{\int_G m(y, \tau_f)\mathrm{d}y} \int_{G \backslash \Omega(t_0)} m(y, \tau_f)\mathrm{d}y, \qquad \text{for all } G \in \sum \left(\bigcup_{\epsilon Y \in \mathcal{P}^*_\epsilon} \epsilon Y \right) \quad (37)$$

where $\sum \left(\bigcup_{\epsilon Y \in \mathcal{P}^*_\epsilon} \epsilon Y \right)$ represents the Borel $\sigma-$algebra of $\bigcup_{\epsilon Y \in \mathcal{P}^*_\epsilon} \epsilon Y$. Locally, in each ϵY, equation (37) is in fact a quantification of the amount of plasmin in $\epsilon Y \backslash \Omega(t_0)$ relative to the total amount of plasmin concentration in ϵY. In conjunction with the

local tissue conditions, this characterises whether the point $x^*_{\epsilon Y}$ is likely to relocate to the new spatial position $\widetilde{x^*_{\epsilon Y}}$ or not.

Now, by assuming that the point $x^*_{\epsilon Y}$ is moved to the position $\widetilde{x^*_{\epsilon Y}}$ if and only if $q^*(x^*_{\epsilon Y}) := q^*(\epsilon Y)$ exceeds a certain threshold $\omega_{\epsilon Y} \in (0, 1)$, we find that the new boundary $\partial\Omega(t_0 + \Delta t)$ will be the interpolation of the following set of points:

$$\{x^*_{\epsilon Y} | \epsilon Y \in \mathcal{P}^*_{\epsilon Y} \text{ and } q(x^*_{\epsilon Y}) < \omega_{\epsilon Y}\} \cup \{\widetilde{x^*_{\epsilon Y}} | \epsilon Y \in \mathcal{P}^*_{\epsilon Y} \text{ and } q(x^*_{\epsilon Y}) \geq \omega_{\epsilon Y}\} \quad (38)$$

Finally before moving to the next time step of the whole macro-micro two-scale system, we replace the initial conditions of the macroscopic dynamics with the solution at the final time of the previous invasion step as follows:

$$\begin{aligned}
c_{\Omega(t_0+\Delta t)}(x, t_0) &:= c(x, t_0 + \Delta t)(\chi_{\Omega(t_0)\setminus \bigcup_{\epsilon Y \in \mathcal{P}^*_\epsilon} \epsilon Y} * \psi_\gamma),\\
v_{\Omega(t_0+\Delta t)}(x, t_0) &:= v(x, t_0 + \Delta t)(\chi_{Y\setminus \bigcup_{\epsilon Y \in \mathcal{P}^*_\epsilon} \epsilon Y} * \psi_\gamma),\\
u_{\Omega(t_0+\Delta t)}(x, t_0) &:= u(x, t_0 + \Delta t)(\chi_{\Omega(t_0)\setminus \bigcup_{\epsilon Y \in \mathcal{P}^*_\epsilon} \epsilon Y} * \psi_\gamma),\\
p_{\Omega(t_0+\Delta t)}(x, t_0) &:= p(x, t_0 + \Delta t)(\chi_{\Omega(t_0)\setminus \bigcup_{\epsilon Y \in \mathcal{P}^*_\epsilon} \epsilon Y} * \psi_\gamma),\\
m_{\Omega(t_0+\Delta t)}(x, t_0) &:= m(x, t_0 + \Delta t)(\chi_{\Omega(t_0)\setminus \bigcup_{\epsilon Y \in \mathcal{P}^*_\epsilon} \epsilon Y} * \psi_\gamma).
\end{aligned} \quad (39)$$

Here $\chi_{\Omega(t_0)\setminus \bigcup_{\epsilon Y \in \mathcal{P}^*_\epsilon} \epsilon Y} * \psi_\gamma$ and $\chi_{Y\setminus \bigcup_{\epsilon Y \in \mathcal{P}^*_\epsilon} \epsilon Y} * \psi_\gamma$ are the characteristic functions corresponding to the sets $\Omega(t_0)\setminus \bigcup_{\epsilon Y \in \mathcal{P}^*_\epsilon} \epsilon Y$ and $Y\setminus \bigcup_{\epsilon Y \in \mathcal{P}^*_\epsilon} \epsilon Y$, and choosing $\gamma \ll \frac{\epsilon}{3}$, $\psi_\gamma : \mathbb{R}^n \to \mathbb{R}_+$ is constructed as a smooth compact support function with $\sup(\psi_\gamma) = \{z \in \mathbb{R}^n | ||z||_2 \leq \gamma\}$. This is defined by the standard mollifier $\psi : \mathbb{R}^n \to \mathbb{R}_+$, namely,

$$\psi_\gamma(x) := \frac{1}{\gamma^n}\psi(\frac{x}{\gamma}), \quad (40)$$

and,

$$\psi(x) := \begin{cases} \dfrac{\exp(\frac{1}{||x||_2^2-1})}{\int_{\{z\in\mathbb{R}^n | ||z||_2 \leq \gamma\}} \exp(\frac{1}{||z||_2^2-1})dz} & \text{if } ||x||_2 < 1,\\ 0 & \text{if } ||x||_2 \geq 1, \end{cases} \quad (41)$$

Then, the invasion process will continue on the new expanded domain $\Omega(t_0)$ with the macroscopic system and the new initial conditions in (39) at macrolevel followed by proteolytic microprocesses around its boundary, which again governs the movement of the boundary of the next time multiscale stage.

Appendix 2: Description of the Multiscale Numerical Approach

We compute and solve the multiscale model in a two-dimensional setting by using computational approach based on a finite difference scheme for macrodynamics and finite element approximation for the microdynamics occurring on each of the boundary ϵY microdomains. In the following subsections, we detail the computational approach and present the steps of the overall multiscale algorithm.

The Macroscopic Stage of the Numerical Scheme

Since the macroscopic dynamics are taking place in the cube Y, we discretise the entire Y by considering a uniform spatial mesh of size $h := \frac{\epsilon}{2}$, i.e. $\Delta x = \Delta y = h$. And, the time interval $[t_0, t_0 + \Delta t]$ is discretised in k uniformly distributed time steps, i.e. using the uniform time step $\delta\tau := \frac{\Delta t}{k}$. The temporal discretisation of the reaction-diffusion system (6)–(10) that we used here is a second-order trapezoidal scheme, while the diffusion term and haptotactic terms are approximated with a second-order midpoint rule. For instance, for the diffusion and haptotactic terms involved in (6), we approximate $\nabla \cdot (\nabla c)^n_{i,j}$ and $\nabla \cdot (c\nabla v)^n_{i,j}$ as follows:

$$\begin{aligned}\nabla\cdot(\nabla c)^n_{i,j} &= \operatorname{div}(\nabla c)^n_{i,j}\\ &\simeq \frac{(c_x)^n_{i+\frac{1}{2},j} - (c_x)^n_{i-\frac{1}{2},j}}{\Delta x} + \frac{(c_y)^n_{i,j+\frac{1}{2}} - (c_y)^n_{i,j-\frac{1}{2}}}{\Delta y},\end{aligned}$$

and

$$\begin{aligned}\nabla\cdot(c\nabla v)^n_{i,j} &= \operatorname{div}(c\nabla v)^n_{i,j}\\ &\simeq \frac{c^n_{i+\frac{1}{2},j}(v_x)^n_{i+\frac{1}{2},j} - c^n_{i-\frac{1}{2},j}(v_x)^n_{i-\frac{1}{2},j}}{\Delta x} + \frac{c^n_{i,j+\frac{1}{2}}(v_y)^n_{i,j+\frac{1}{2}} - c^n_{i,j-\frac{1}{2}}(v_y)^n_{i,j-\frac{1}{2}}}{\Delta y},\end{aligned}$$

where

$$\begin{cases} c^n_{i,j+\frac{1}{2}} := \frac{c^n_{i,j}+c^n_{i,j+1}}{2},\\ c^n_{i,j-\frac{1}{2}} := \frac{c^n_{i,j}+c^n_{i,j-1}}{2},\\ c^n_{i+\frac{1}{2},j} := \frac{c^n_{i,j}+c^n_{i+1,j}}{2},\\ c^n_{i-\frac{1}{2},j} := \frac{c^n_{i,j}+c^n_{i-1,j}}{2},\end{cases}$$

are the midpoint approximations for c and

$$\begin{cases} (c_y)^n_{i,j+\frac{1}{2}} := \frac{c^n_{i,j+1}-c^n_{i,j}}{\Delta y}, \\ (c_y)^n_{i,j-\frac{1}{2}} := \frac{c^n_{i,j}-c^n_{i,j-1}}{\Delta y}, \\ (c_x)^n_{i+\frac{1}{2},j} := \frac{c^n_{i+1,j}-c^n_{i,j}}{\Delta x}, \\ (c_x)^n_{i-\frac{1}{2},j} := \frac{c^n_{i,j}-c^n_{i-1,j}}{\Delta x}, \end{cases}, \quad \text{and} \quad \begin{cases} (v_y)^n_{i,j+\frac{1}{2}} := \frac{v^n_{i,j+1}-v^n_{i,j}}{\Delta y}, \\ (v_y)^n_{i,j-\frac{1}{2}} := \frac{v^n_{i,j}-v^n_{i,j-1}}{\Delta y}, \\ (v_x)^n_{i+\frac{1}{2},j} := \frac{v^n_{i+1,j}-v^n_{i,j}}{\Delta x}, \\ (v_x)^n_{i-\frac{1}{2},j} := \frac{v^n_{i,j}-v^n_{i-1,j}}{\Delta x}, \end{cases}$$

represent the central differences for spatial derivatives of c and v. Note that $n = 0, 1, ..., k$ are index of time step and (i, j) are spatial nodes where $i = 1, ...q$ are the indices for the x-direction and $j = 1, ...q$ are the indices for the y-direction. The diffusion terms in Eqs. (8)–(10) are approximated in the same way as it is in Eqs. (6) and (7).

The Computational Microscopic Scheme and Its Relation to the Macroscopic Level

In this section, we describe our computational scheme for the micro scale dynamics occurring on each microdomains $\epsilon Y \in \mathcal{P}^*_\epsilon$, which are cubes of size ϵ located at the boundary $\partial\Omega(t_0)$. We have each microdomain ϵY centred at a boundary point form the macroscopic mesh, with the neighbouring ϵ-cubes staring from the centre of the current one (i.e. they are appropriately "half-way shifted" copies of $\epsilon Y \in \mathcal{P}^*_\epsilon$), due to the purposely chosen macroscopic mesh size $h = \frac{\epsilon}{2}$ and the properties of the family $\mathcal{P}^*_{\epsilon Y}$. Moreover, the centre point of the microdomains is coincidentally the midpoint induced by ϵY on $[\partial\Omega(t_0)]_{\epsilon Y}$, i.e. $x^*_{\epsilon Y}$.

In order to compute the integrals in the source terms (i.e. $f_1^{\epsilon Y}$ and $f_2^{\epsilon Y}$) in the microscopic system (12)–(15), a midpoint rule is proposed and the constitutive details are given below. Assuming that K denotes a generic element domain in a finite element subdivision with either triangular or square elements of a given region $A \subset \mathbb{R}^2$, this "midpoint rule" consists of approximating the integral of a function f over K as the product between the value of f at the centre of mass of K, K_{centre}, and the Lebesgue measure of K, namely,

$$\int_K f = f(K_{\text{centre}})\lambda(K). \tag{42}$$

For an arbitrarily chosen $\epsilon Y \in \mathcal{P}^*_\epsilon$, we consider a finite element approach involving triangular elements on a uniform micromesh, which is maintained with identical structure for all the microdomains. Further, we consider a time-constant approximation $\tilde{f}_1^{\epsilon Y}$ of $f_1^{\epsilon Y}$ on the time interval $[0, \Delta t]$. In this context, using the computed final-time values of $c(\cdot, t_0 + \Delta t)$ at the macromesh points that are included on the current microdomain, $x_1, x_2, ..., x_{P_{\epsilon Y}} \in \epsilon Y \cap \Omega(t_0)$, we take:

$$\tilde{f}_1^{\epsilon Y}(x_s) = \frac{1}{\lambda(B(x_s, 2\epsilon) \cap \Omega(t_0))} \int_{B(x_s,2\epsilon)\cap\Omega(t_0)} c\ (x_s, t_0 + \Delta t)\ \mathrm{d}x, \tag{43}$$

where $s = 1, ..., P_{\epsilon Y}$, and the integrals are computed via the midpoint rule. For the rest of the points y on the micromesh, the value of $\tilde{f}_1^{\epsilon Y}$ is obtained in terms of the set of finite element basis functions considered at the contact points, i.e. $\{\phi_{x_s} | s = 1, ..., P_{\epsilon Y}\}$. Finally, we observe that for any micromesh point $y \in \epsilon Y$ we have two possibilities:

Case 1 If there exists three overlapping points $x_{i_1}, x_{i_2}, x_{i_3} \in \{x_1, x_2, ..., x_{P_{\epsilon Y}}\}$ which belongs to the same connected component of $\epsilon Y \cap \Omega(t_0)$ and y belongs to the convex closure of the set, i.e. $y \in \text{Conv}\{x_{i_1}, x_{i_2}, x_{i_3}\}$, then we have:

$$\tilde{f}_1^{\epsilon Y}(y) = \tilde{f}_1^{\epsilon Y}(x_{i_1})\phi_{x_{i_1}}(y) + \tilde{f}_1^{\epsilon Y}(x_{i_2})\phi_{x_{i_2}}(y) + \tilde{f}_1^{\epsilon Y}(x_{i_3})\phi_{x_{i_3}}(y). \tag{44}$$

Case 2 If y does not satisfy the conditions in Case 1, then we have

$$\tilde{f}_1^{\epsilon Y}(y) = 0. \tag{45}$$

For the source term $f_2^{\epsilon Y}$, we use the same approximation method as above, except that there is only one case taken into consideration which is similar in Eq. (44) according to the definition of $f_2^{\epsilon Y}$. Now we could obtain the source terms $\tilde{f}_1^{\epsilon Y}$ and $\tilde{f}_2^{\epsilon Y}$ on each microdomain ϵY with zero initial condition and Neumann boundary conditions and furthermore use the finite element method to solve the reaction-diffusion equations (12)–(15) on ϵY over the time interval $[0, t_0 + \Delta t]$. Then, we use bilinear elements on a square mesh, the numerical scheme for the microprocesses occurring on each ϵY is finally obtained by involving a trapezoidal predictor-corrector method for the time integration.

Then, for each microdomain we use the midpoint rule to compute the transitional probability described in (37). For simplicity, now the numerical implementation of the multiscale model for cancer invasion proposed above is slightly simplified in the following way: provided that the transitional probability exceeds an associated threshold $\omega_{\epsilon Y} \in (0, 1)$, the boundary mesh-point $x^*_{\epsilon Y}$ will move in direction $\eta_{\epsilon Y}$ to the macromesh point from $\partial\epsilon Y \backslash [\Omega(t_0)]_{\epsilon Y}$ that is closest (in Euclidean distance) to $x^*_{\epsilon Y}$. If the threshold is not satisfied, then $x^*_{\epsilon Y}$ remains at the same spatial location. Therefore, the new boundary $\partial\Omega(t_0 + \Delta t)$ is now obtained by the interpolation of the set of points given in (38) , and the computational process is continued on the new domain $\Omega(t_0 + \Delta t)$ by using as a discretised version of (39) as a new initial condition at the macroscopic stage, i.e.

$$c(x_{i,j}, t_0 + \Delta t) = \begin{cases} c^k_{i,j}, & x_{i,j} \in \overline{\Omega(t_0)}, \\ \frac{1}{4}(c^k_{i-1,j} + c^k_{i+1,j} + c^k_{i,j-1} + c^k_{i,j+1}), & x_{i,j} \in \overline{\mathbf{B}(\overline{\Omega(t_0)}, h)} \backslash \overline{\Omega(t_0)}, \\ 0, & x_{i,j} \notin \overline{\mathbf{B}(\overline{\Omega(t_0)}, h)}, \end{cases} \tag{46}$$

and,

$$\begin{aligned} v(x_{i,j}, t_0 + \Delta t) &= v_{i,j}^k, & u(x_{i,j}, t_0 + \Delta t) &= u_{i,j}^k, \\ p(x_{i,j}, t_0 + \Delta t) &= p_{i,j}^k, & m(x_{i,j}, t_0 + \Delta t) &= m_{i,j}^k. \end{aligned} \tag{47}$$

where $\{x_{i,j}\ i, j = 1, ..., q\}$ is the macroscopic mesh in Y, $\overline{\Omega(t_0)}$ is the topological closure of $\Omega(t_0)$, and $\mathbf{B}(\overline{\Omega(t_0)}, h)$ represents the topological closure of the h-bundle of $\overline{\Omega(t_0)}$., i.e. $\mathbf{B}(\overline{\Omega(t_0)}, h) := \{x \in Y | \exists z_x \in \overline{\Omega(t_0)}$ such that $||x - z_x||_2 \leq h\}$.

Overall Algorithm Steps

To sum up, the overall algorithm package of the macromicroscopic method consists of the following steps:

Step 1 At the very begining time t_0, first of all, we discretise the macrodomain $[a, b] \times [c, d]$ by

$$\begin{aligned} a = x_0, \ldots, x_i = a + i\Delta x, \ldots, x_m = a + m\Delta x = b, \\ c = y_0, \ldots, y_j = c + j\Delta y, \ldots, y_n = c + n\Delta y = d. \end{aligned}$$

where $\Delta x = \Delta y = h$, $h := \frac{\epsilon}{2}$ and let $a = c = 0, c = d = 4$. Also, we number each point on the macrodomain and record their coordinates all sorts of data of the domain that might be used later.

Step 2 Define initial conditions for cancer and ECM distribution on macrodomain:

$$\begin{aligned} c(x, t_0) &=: c_0(x), & x &\in \Omega(t_0) \\ v(x, t_0) &=: v_0(x), & x &\in \Omega(t_0) \\ u(x, t_0) &=: u_0(x), & x &\in \Omega(t_0) \\ p(x, t_0) &=: p_0(x), & x &\in \Omega(t_0) \\ m(x, t_0) &=: m_0(x), & x &\in \Omega(t_0) \end{aligned}$$

where $c(x, t_0)$ is set as zero at the mesh points located outside the closure of the macroscopic domain $\Omega(t_0)$.

Step 3 Start the main time loop (from time stage 1 to certain time stage N), and at the current time stage,

a) Run the macrosolver, which applies the finite difference scheme mentioned above, to obtain the distribution of components in the system $c_{i,j}^{n+1}$ $v_{i,j}^{n+1}$, $u_{i,j}^{n+1}$, $p_{i,j}^{n+1}$, and $m_{i,j}^{n+1}$, where $i, j = 1, ..., q$.

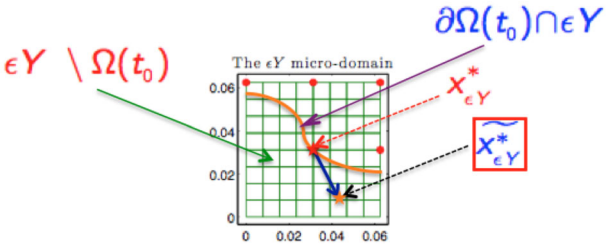

Fig. 13 Plot shows the relocation of one point on the boundary moves to a new spatial position in the microdomain ϵY

b) Run the microsolver, in which we loop over each points that was on the boundary of tumour at previous time, and at an arbitrary boundary points,
   i. Define the microdomain ϵY centring at the current point on the boundary, which consists of nine points on macrodomain. For simplicity, we first construct the domain on $[0, \epsilon]\times[0, \epsilon]$, and on this domain, compute the source terms $f_1^{\epsilon Y}$ and $f_2^{\epsilon Y}$, and by interpolation, we uniformly decompose the domain into sixty-four square elements which consists of eighty-one points in total, with the source term values and concentration values for uPA, PAI-1 and plasmin on a finer mesh (see Fig. 13).
   ii. On the microdomain ϵY, apply the finite element method to solve the microscopic dynamics system (12)–(15), to obtain the spatial distribution of plasmin at the final microtime $m(\cdot, \tau_f)$ (involving a proposed midpoint rule formula for the integral source terms $f_1^{\epsilon Y}$ and $f_2^{\epsilon Y}$, and for time integration a trapezoidal predictor-corrector), which will be used in the regulation functions of cancer cells' movement.
   iii. Translated the coordinates on this microdomain back to where the microspatial position was before.
   iv. Using the transitional probability q^* defined in (37), compute the invasion strength as $q^*(x^*_{\epsilon Y}) := q^*(\epsilon Y)$.
   v. If and only if the microenvironment induced probability $q^*(x^*_{\epsilon Y})$ is greater than some tissue threshold value $\omega_{\epsilon Y} \in (0, 1)$, we further compute the direction $\eta_{\epsilon Y}$ and magnitude $\xi_{\epsilon Y}$ of the movement as described by (35) and (36).

c) Once finishing both macrosolver and microsolver at the current time stage, we obtained new macroscopic distribution for each components in the system $c_{i,j}^{n+1}$, $v_{i,j}^{n+1}$, $u_{i,j}^{n+1}$, $p_{i,j}^{n+1}$ and $m_{i,j}^{n+1}$; also for each midpoint $x^*_{\epsilon Y}$ on the tumour boundary, we have the possibility $q^*(x^*_{\epsilon Y})$, direction $\eta_{\epsilon Y}$ and magnitude $\xi_{\epsilon Y}$ of their movement; therefore, we could use all these information to determine the new position $\widetilde{x^*_{\epsilon Y}}$ and the points remain where they were on the cancer interface $\partial\Omega(t_0 + \Delta t)$. This is schematically shown in Fig. 13
   where the red dots represent the discrete macromesh location for the where microscale source induced by the macroscale was calculated via the integral formula (43).

d) Finally, by using approximations shown in (46) and (47), replace the initial values of cancer and ECM distribution in macroscopic dynamics with the solution at the final time of the previous macrostep.

Step 4 Using the new initial conditions for macroscopic dynamics, continue the invasion process by coupling the next-step macroprocess given by the systems (6) and (10) on the expand domain $\Omega(t_0 + \Delta t)$ with the corresponding microprocesses (12)–(15) occurring on its boundary, which means repeating the Step 3 above with new initial conditions for macroscopic dynamics and new boundary of cancer.

Appendix 3: Table for the Parameter Set $\mathscr{P}$

In Table 1, we present a description of the parameters included in $\mathscr{P}$.

Table 1 The parameters in $\mathscr{P}$

Parameter	Value	Description
D_c	4.3×10^{-3}	Diffusion of cancer cells
χ_u	3.05×10^{-2}	Chemotaxis to uPA
χ_p	3.75×10^{-2}	Chemotaxis to PAI-1
χ_v	2.85×10^{-2}	Haptotaxis to ECM(vitronectin)
μ_1	0.25	Proliferation of cancer cells
δ	1.5	Degradation of ECM
ϕ_{21}	0.75	Binding of uPA and PAI-1
ϕ_{22}	0.55	Binding of PAI-1 and VN
μ_2	0.01	Proliferation of ECM
D_u	2.5×10^{-3}	Diffusion of uPA
ϕ_{31}	0.75	Binding of uPA of PAI-1
ϕ_{33}	0.3	Binding of uPA and uPAR
α_{31}	0.215	Production of uPA
D_p	3.5×10^{-3}	Diffusion of PAI-1
ϕ_{41}	0.75	Binding of uPA and PAI-1
ϕ_{42}	0.55	Binding of PAI-1 and VN
α_{41}	0.5	Production of PAI-1
D_m	4.91×10^{-3}	Diffusion of plasmin
ϕ_{52}	0.11	Increase rate due to binding of PAI-1 and VN
ϕ_{53}	0.75	Increase rate due to binding of uPA and uPAR
ϕ_{54}	0.5	Degradation of plasmin

References

Abdulle A, Schwab C (2005) Heterogeneous multiscale fem for diffusion problems on rough surfaces. Multiscale Model Simul 3(1):195–220

Adam JA (1986) A simplified mathematical model of tumour growth. Math Biosci 81(2):229–244

Allaire G (1992) Homogenization and two-scale convergence. SIAM J Math Anal 23(6):1482–1518

Andasari V, Gerisch A, Lolas G, South A, Chaplain MAJ (2011) Mathematical modeling of cancer cell invasion of tissue: biological insight from mathematical analysis and computational simulation. J Math Biol 63(1):141–171

Anderson A, Chaplain M, Newman E, Steele R, Thompson A (2000) Mathematical modelling of tumour invasion and metastasis. J Theor Med 2:129–154

Anderson ARA (2005) A hybrid mathematical model of solid tumour invasion: the importance of cell adhesion. Math Med Biol 22:163–186

Andreasen P, Kjøller L, Christensen L, Duffy M (1997) The urokinase-type plasminogen activator system in cancer metastasis: a review. Int J Cancer 72:1–22

Andreasen P, Egelund R, Petersen H (2000) The plasminogen activation system in tumor growth, invasion, and metastasis. Cell Mol Life Sci 57:25–40

Armstrong NJ, Painter KJ, Sherratt JA (2006) A continuum approach to modelling cell-cell adhesion. J Theor Biol 243(1):98–113

Aubert M, Badoual M, Féreol S, Christov C, Grammaticos B (2006) A cellular automaton model for the migration of glioma cells. Phys Biol 3(2):93

Byrne H, Chaplain M, Pettet G, Mcelwain DLS (2001) A mathematical model of trophoblast invasion. Appl Math Lett 14(8):1005–1010

Byrne HM, Chaplain MA (1996) Modelling the role of cell–cell adhesion in the growth and developement of carcinoma. Math Comput Model 24(12):1–17

Byrne HM, Chaplain MAJ (1997) Free boundary value problems associated with the growth and development of multicellular spheroids. Eur J Appl Math 8:639–658

Byrne H, Preziosi L (2003) Modelling solid tumour growth using the theory of mixtures. Math Med Biol 20:341–366

Chaplain M, Graziano L, Preziosi L (2006) Mathematical modelling of the loss of tissue compression responsiveness and its role in solid tumour development. Math Med Biol 23:197–229

Chaplain M, McDougal S, Anderson A (2006) Mathematical modeling of tumor-induced angiogenesis. Annu Rev Biomed Eng 8:233–257

Chaplain M, Lachowicz M, Szymanska Z, Wrzosek D (2011) Mathematical modelling of cancer invasion: the importance of cell–cell adhesion and cell-matrix adhesion. Math Model Methods Appl Sci 21(4):719–743

Chaplain M, Lolas G (2005) Mathematical modelling of cancer cell invasion of tissue: the role of the urokinase plasminogen activation system. Math Model Methods Appl Sci 15(11):1685–1734

Chaplain M, Lolas G (2006) Mathematical modelling of cancer invasion of tissue: dynamic heterogeneity. Netw Heterog Media 1:399–439

Cristini V, Lowengrub J, Nie Q (2003) Nonlinear simulation of tumour growth. J Math Biol 46:191–224

Dass K, Ahmad A, Azmi A, Sarkar S, Sarkar F (2008) Evolving role of uPA/uPAR system in human cancers. Cancer Treat Rev 34:122–136

Deakin NE, Chaplain MAJ (2013) Mathematical modelling of cancer cell invasion: the role of membrane-bound matrix metalloproteinases. Front Oncol 3(70):1–9

Degryse B, Sier C, Resnati M, Conese M, Blasi F (2001) PAI-1 inhibits urokinase-induced chemotaxis by internalizing the urokinase receptor. FEBS Lett 505:249–254

Deisboeck TS, Wang Z, Macklin P, Cristini V (2011) Multiscale cancer modeling. Annu Rev Biomed Eng 13:127–155

Domschke P, Trucu D, Gerisch A, Chaplain M (2014) Mathematical modelling of cancer invasion: implications of cell adhesion variability for tumour infiltrative growth patterns. J Theor Biol 361:41–60

E W, Engquist B (2003) The heterogeneous multiscale methods. Comm Math Sci 1:87–132

Frieboes HB, Zheng X, Sun CH, Tromberg B, Gatenby R, Cristini V (2006) An integrated computational/experimental model of tumor invasion. Cancer Res 66:1597–1604

Frieboes HB, Lowengrub JS, Wise S, Zheng X, Macklin P, Bearer EL, Cristini V (2007) Computer simulation of glioma growth and morphology. NeuroImage 37(Supplement 1):S59–S70

Frieboes HB, Jin F, Chuang YL, Wise SM, Lowengrub JS, Cristini V (2010) Three-dimensional multispecies nonlinear tumor growth—ii: tumor invasion and angiogenesis. J Theor Biol 264:1254–1278
Gatenby RA, Gawlinski ET, Gmitro AF, Kaylor B, Gillies RJ (2006) Acid-mediated tumor invasion: a multidisciplinary study. Cancer Res 66:5216–5223
Gatenby RA, Gawlinski ET (1996) A reaction-diffusion model of cancer invasion. Cancer Res 56:5745–5753
Gerisch A, Chaplain M (2008) Mathematical modelling of cancer cell invasion of tissue: local and non-local models and the effect of adhesion. J Theor Biol 250:684–704
Greenspan HP (1976) On the growth and stabiligy of cell cultures and solid tumours. J Theor Biol 56:229–242
Halmos P (1974) Measure theory. Springer, New York
Hanahan D, Weinberg RA (2000) The hallmarks of cancer. Cell 100:57–70
Hanahan D, Weinberg RA (2011) The hallmarks of cancer: the next generation. Cell 144:646–674
Hillen T, Painter K, Winkler M (2013) Convergence of a cancer invasion model to a logistic chemotaxis model. Math Model Methods Appl Sci 23:165–198
Ito E, Ozawa S, Kijima H, Kazuno A, Nishi T, Chino O, Shimada H, Tanaka M, Inoue S, Inokuchi S, Makuuchi H (2012) New invasive patterns as a prognostic factor for superficial esophageal cancer. J Gastroenterol 47:1279–1289
Joyce JA, Pollard J (2009) Microenvironmental regulation of metastasis. Nat Rev Cancer 9(4):239–252
Kalluri R, Zeisberg M (2006) Fibroblasts in cancer. Nat Rev Cancer 6(5):392–401
Kolbe N, Katuchova J, Sfakianakis N, Hellmann N, Lukacova-Medvidova M (2014) Numerical study of cancer cell invasion dynamics using adaptive mesh refinement: the urokinase model. arXiv preprint arXiv:1408.0642
Lin P (2007) Convergence analysis of a quasi-continuum approximation for a two-dimensional material without defects. SIAM J Numer Anal 45(1):313–332
Macklin P, McDougall S, Anderson ARA, Chaplain MAJ, Cristini V, Lowengrub J (2009) Multiscale modelling and nonlinear simulation of vascular tumour growth. J Math Biol 58:765–798
Macklin P, Lowengrub J (2005) Evolving interfaces via gradients of geometry-dependent interior poisson problems: application to tumor growth. J Comput Phys 203(1):191–220
Macklin P, Lowengrub J (2006) An improved geometry-aware curvature discretization for level set methods: application to tumor growth. J Comput Phys 215(2):392–401
Macklin P, Lowengrub J (2007) Nonlinear simulation of the effect of microenvironment on tumor growth. J Theor Biol 245(4):677–704
Macklin P, Lowengrub J (2008) A new ghost cell/level set method for moving boundary problems: application to tumor growth. J Sci Comput 35:266–299
Masuda R, Kijima H, Imamura N, Aruga N, Nakamura Y, Masuda D, Takeichi H, Kato N, Nakagawa T, Tanaka M, Inokuchi S, Iwazaki M (2012) Tumor budding is a significant indicator of a poor prognosis in lung squamous cell carcinoma patients. Mol Med Rep 6(5):937–943
Painter KJ, Hillen T (2011) Spatio-temporal chaos in a chemotaxis model. Phys D 240:363–375
Perumpanani A, Sherratt J, Norbury J, Byrne H (1996) Biological inferences from a mathematical model for malignant invasion. Invasion Metastasis 16(4–5):209–221
Perumpanani A, Simmons D, Gearing A, Miller K, Ward G, Norbury J, Schneemann M, Sherratt J (1998) Extracellular matrix-mediated chemotaxis can impede cell migration. Proc R Soc Lond B 265(1413):2347–2352
Popławski NJ, Agero U, Gens JS, Swat M, Glazier JA, Anderson ARA (2009) Front instabilities and invasiveness of simulated avascular tumors. Bull Math Biol 71:1189–1227
Preziosi L, Tosin A (2009) Multiphase modelling of tumour growth and extracellular matrix interaction: mathematical tools and applications. J Math Biol 58:625–656
Qian BZ, Pollard JW (2010) Macrophage diversity enhances tumor progression and metastasis. Cell 141(1):39–51
Ramis-Conde I, Drasdo D, Anderson AR, Chaplain MA (2008) Modeling the influence of the E-cadherin-β-catenin pathway in cancer cell invasion: a multiscale approach. Biophys J 95(1):155–165
Ren W, E W (2005) Heterogeneous multiscale method for the modeling of complex fluids and micro-fluidics. J Comp Phys 204(1):1–26
Resnati M, Pallavicini I, Wang J, Oppenheim J, Serhan C, Romano M, Blasi F (2002) The fibrinolytic receptor for urokinase activates the G protein-coupled chemotactic receptor FPRL1/LXA4R. Proc Natl Acad Sci Am 99:1359–1364

Roussos E, Condeelis J, Patsiaiou A (2011) Chemotaxis in cancer. Nat Rev Cancer 11:573–587
Rubenstein BM, Kaufman LJ (2008) The role of extracellular matrix in glioma invasion: a cellular potts model approach. Biophys J 95(12):5661–5680
Sabeh F, Shimizu-Hirota R, Weiss SJ (2009) Protease-dependent versus -independent cancer cell invasion programs: three-dimensional amoeboid movement revisited. J Cell Biol 185(1):11–19
Smith HW, Marshall CJ (2010) Regulation of cell signalling by upar. Nat Rev Mol Cel Biol 11:23–36
Stetler-Stevenson WG, Aznavoorian S, Liotta LA (1993) Tumor cell interactions with the extracellular matrix during invasion and metastasis. Annu Rev Cell Biol 9:541–573
Tang L, Han X (2013) The urokinase plasminogen activator system in breast cancer invasion and metastasis. Biomed Pharmacother 67:179–182
Tektonidis M, Hatzikirou H, Chauvière A, Simon M, Schaller K, Deutsch A (2011) Identification of intrinsic in vitro cellular mechanisms for glioma invasion. J Theor Biol 287:131–147
Trucu D, Chaplain M, Marciniak-Czochra A (2012) Three-scale convergence for processes in heterogeneous media. Appl Anal 91(7):1351–1373
Trucu D, Lin P, Chaplain MAJ, Wang Y (2013) A multiscale moving boundary model arising in cancer invasion. Multiscale Model Simul 11(1):309–335
Venkatraman L, Chia SM, Narmada BC, White JK, Bhowmick SS Jr, Dewey CF, So PT, Tucker-Kellogg L, Yu H (2012) Plasmin triggers a switch-like decrease in thrombospondin-dependent activation of TGF-β1. Biophys J 103(5):1060–1068
Webb S, Sherratt J, Fish R (1999) Alterations in proteolytic activity at low pH and its association with invasion: a theoretical model. Clin Exp Metastasis 17(5):397–407
Wise S, Lowengrub J, Friebose H, Cristini V (2008) Three-dimensional multispecies nonlinear tumor growth—i: model and numerical method. J Theor Biol 253(3):524–543
Wise SM, Lowengrub J, Christini V (2011) An adaptive multigrid algorithm for simulating solid tumor growth using mixture models. Math Comput Model 53:1–20
Zheng X, Wise S, Cristini V (2005) Nonlinear simulation of tumor necrosis, neo-vascularization and tissue invasion via an adaptive finite-element/level-set method. Bull Math Biol 67(2):211–259